An Experimental Analysis of the Characteristic Behaviors of an Impedance Pump

Thesis by

Anna Iwaniec Hickerson

In Partial Fulfillment of the Requirements

for the Degree of

Doctor of Philosophy

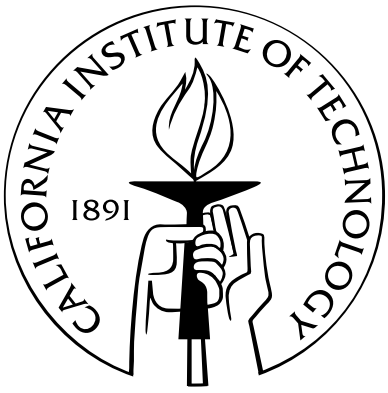

California Institute of Technology

Pasadena, California

2005

(Defended April 28, 2005)

For my hubby, Kevin, with all my love.

Acknowledgements

I would like to thank all the people who supported me throughout graduate school and the writing of my thesis. Special thanks go to my advisor, Prof. Mory Gharib for his insight, inspiration, and motivation and my committee — Prof. Mory Gharib, Prof. John Brady, Prof. Joel Burdick, and Prof. Michael Dickinson — for their time, expertise, advice and direction. Additional thanks go to all the members of the group. Through fun times and hard times, it felt as though we were a family, without which the experience would be empty.

My heartfelt thanks go to my parents for showing me the value of education through reason and example and to my friend Jeanne, for being with me through the hardest times of growing up, letting me be the geek that I am, and telling me about a small school in California I might be interested in.

Lastly, I would like to give thanks to the Fehrer Fellowship for providing financial support for my research.

Abstract

When a fluid-filled pliant tube is connected to tubing of a different impedance, a net flow in either direction can be induced by periodically compressing the pliant section asymmetrically from the ends. An experimental analysis of the characteristic behaviors of such a pump has been done demonstrating interesting results not predicted by prior analytical and computational results. Measurements show a complex non-linear behavior in response to the compression frequency, including distinct resonance peaks and reversals in flow direction. Ultrasound imaging provided a unique view of the tube wall and flow within, allowing us to visualize the wave propagation and reflection. Measurements include transient responses, resonant responses, and bulk flow behaviors for a variety of configurations. Net flow rates can exceed the volumetric displacement done by active compression demonstrating that, as a first approximation, this pump can have a higher efficiency than peristaltic pumping. Elasticity has been shown not to be a necessary factor in stimulating net forward flow.

Results from this study have helped show that a zebrafish (a model for human cardiac development) may utilize impedance pumping to drive circulation in early embryonic stages prior to valve formation as opposed to peristaltic pumping as was once thought. Additional research is being conducted to develop a micro-scaled version with applications in medicine, heat transfer, lab-on-chip technology, and micromixing.

Contents

Chapter 1

Introduction

The process of fluid transport plays a critical role in fulfilling two fundamental requirements for sustaining life: obtaining food and disposing of waste. Depending on environment and scale, there are two fundamental approaches that can be used to accomplish these tasks: move the body through the fluid, such as in swimming and flying; and move the fluid through the body, such as in digestion, breathing, and heat transport.

To move fluid we need pumps, be it our own beating hearts or our intestines, or other solutions nature has devised such as wings, jellyfish jets, gopher burrows, and flagella [33]. With all the diversity and complexity that nature has evolved in its pump designs, certain features, though not without exception, remain simple: flexible membranes, lack of blades, and lack of valves. These features eliminate mechanical complexity that is prone to failure. Even the human heart establishes unidirectional circulation prior to the formation of valves.

1.1 Pumping Mechanisms

Pumps in bioengineering can be divided into two broad categories: man made pumps used for biological research and biomedical applications, and naturally occurring pumps in biological systems. In most cases, these will overlap. The impedance pump is no exception. Biological systems can provide insight into the development of artificial pumps, and artificial pumps can prove to be models for naturally occurring

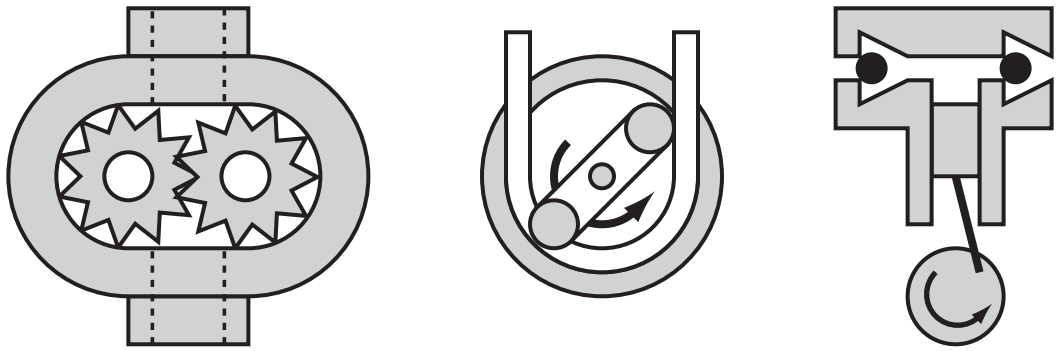

(a) Gear pump (b) Peristaltic pump (c) Piston pump

Figure 1.1: Example positive displacement pumps

systems. Some of the more prominent fluid transport mechanisms include positive displacement pumps and dynamic pumps.

1.1.1 Positive Displacement Pumps

Positive displacement pumps function by filling a chamber with fluid and displacing the volume. Among the more common positive displacement pumps are peristaltic and reciprocating pumps. These type of pumps are not dependent on the pressure head or viscosity. The stroke to volume ratio is constant. That means that they have a linear response to the driving frequency, be it a motor or a piston. They typically produce low flow rates at high pressures.

A peristaltic pump consists of a tube or channel that is first compressed at one location, and then the compression is moved along the length of the channel, displacing the fluid that was in front of it. It is primarily used for moving highly viscous fluids that are either corrosive, or cannot be contaminated. The intestines are an example of such a pumping mechanism.

A reciprocating pump has two one-way valves, and a chamber that is filled and displaced between the two valves by a piston or membrane moving in a reciprocating motion. Other variations of positive displacement pumps include a gear pump, peristaltic pump and piston pump (figure 1.1).

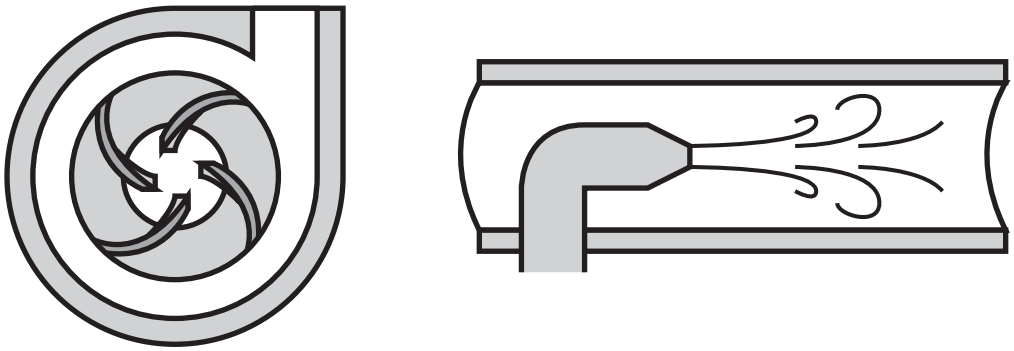

(a) Centrifugal pump (b) Jet pump

Figure 1.2: Example kinetic pumps

1.1.2 Dynamic Pumps

Dynamic pumps function by transferring kinetic energy to the fluid in such a way as to create a pressure head. For example, a centrifugal pump consists of a set of rotating vanes that impart kinetic energy into the fluid. The vanes or blades rely on the Bernoulli effect to create a pressure across them (figure 1.2(a)). It is the most common pump used in engineering applications though it is not found in this form in nature. A jet pump is a classic example of a kinetic pump that does not use vanes or blades. A jet of fluid is directed into a pipe that transfers its kinetic energy into the fluid, causing it to flow (figure 1.2(b)).

1.1.3 Impedance Pump

Impedance is defined as the resistance of a medium to the transmission of a wave, and is dependent on the frequency components of the wave being transmitted. Whenever two mediums connect that have different impedances, a wave passing through that intersection will partially reflect in an amount based on the relative values of those impedances. This is true for electrical signals crossing different wires, for pressure waves moving into different densities, and for mechanical waves in a string.

An impedance pump can then be defined as a fluid-filled pliant tube, open and connected at the ends to tubing of a different impedance such that when a wave

travels along the surface of the pliant section there will be at least partial reflection of the wave at the impedance mismatched interface. When this pliant section is periodically compressed off-center from the interfaces to the different tubing, a net flow can occur. The impedance pump functions by imparting the kinetic energy by the action of compression and transmitting that energy via surface waves into the fluid to build a pressure head, thus making it another example of a kinetic pump that does not require vanes (figure 1.3).

It has recently been shown that the impedance pump may serve as a model of heart function in the early embryonic stages of vertebrae before valve or chamber development [5] as opposed to peristaltic pumping as was once thought [4]. In vivo observations and analysis show a number of non-peristaltic characteristics found in the impedance pump. These include pulsatile flow, retrograde flow, a non-linear response of the net flow rate to the frequency of pinching, wave reflection, and wave dissipation.

The hypothesis can be further extended to the aortic vessels of an adult. Many studies have been done on the passive elastic properties of these vessels [6, 11, 12, 25, 27, 28, 34–39] and how these properties may help reduce the power required for circulation. In the case of a diseased individual who may have hardening of the vessels, they may lose the benefit of this pumping and perhaps even have a reverse effect [7]. The impedance pump may both provide insight into the passive properties and become a medical device used in the treatment of the arterial diseases [24].

Additional research is being conducted to develop a micro-scaled version [30] with applications in medicine, heat transfer, lab-on-chip technology, and micro-mixing.

1.2 Prior Work

In 1954, Gerhart Liebau demonstrated valveless pumping (figure 1.4) [18–20] by periodically compressing and elastic tube and showed that it was able to pump fluid from a lower to a higher pressure head. Liebau suggested that elasticity, viscosity, and inertia affected the performance of the device. But he was not able to explain

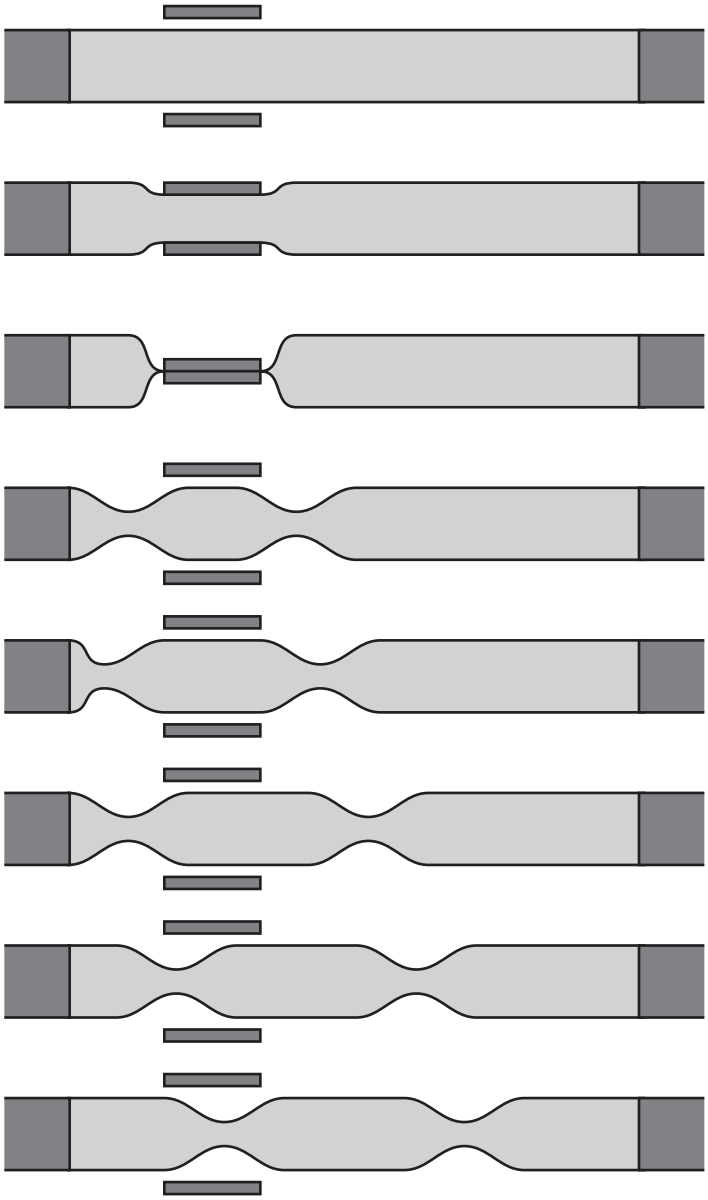

Figure 1.3: Impedance pump diagram

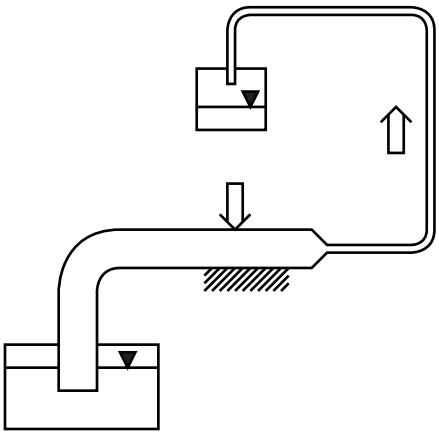

Figure 1.4: Liebau's model of the impedance pump

how these parameters contributed to the pumping [18, 23].

Since his work, there has been a large collection of analytical [1, 16, 17, 23, 26, 29, 32, 40] and computational [2, 13–15] studies that attempt to describe the phenomena. However, there have been very few experimental studies [18, 22, 26], most of which were limited to validating one or two cases to complement their analytical and computational work.

By 1978, Hans Thomann had developed a mathematical model of the pumping mechanism with simplifying assumptions [32]. The model was of a torus that can be cut open and treated as a periodic entity (figure 1.5). His model is for one-dimensional, periodic, inviscid, and incompressible flow. He assumed the volume displaced for each compression is divided equally to either side of the compression. He further assumed a fixed relationship between the pressure within the tube, p, and the cross-sectional area, A with constants c_1, c_2 and n.

$$p = c_1 + c_2 A^n$$

These assumptions were used to simplify the Navier-Stokes equations and continuity equation. He further simplified the governing equations by linearizing them, and solving them using the method of characteristics. In order to impose boundary con-

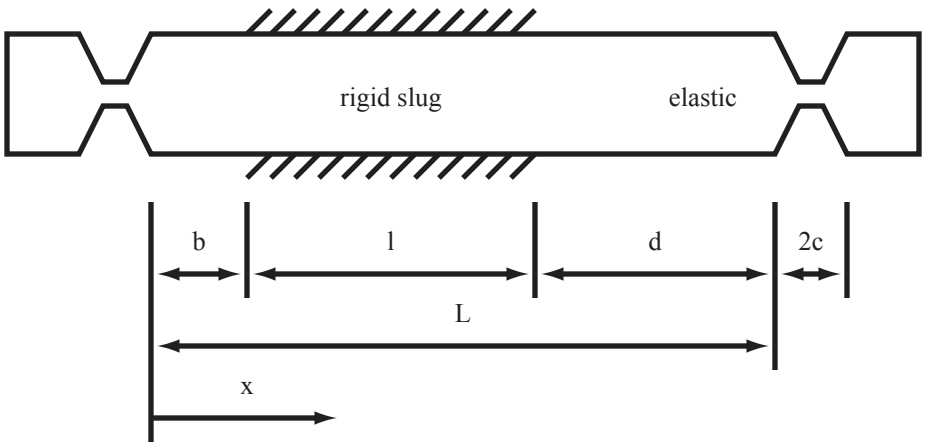

Figure 1.5: Thomann's model of the impedance pump

ditions, Thomann assumed a rigid tube connected the ends of the pump forces the flow and pressure to match at the ends of the pump.

Thomann's model shows that a net flow can be induced. His assumptions, however, greatly limit the usefulness of his results. His model required the inertial force of the fluid in the rigid connecting loop to oscillate and therefore create a net flow. Also, by linearizing the equations, he got results that are only valid for small deformations of the elastic surface. This effectively means his solutions are only valid for elastic wall deformations with long wavelengths.

Another model of the impedance pump was presented by Maximilian Moser in 1998 [23]. He suggested that the impedance pump need not be a tube, but rather two distensible reservoirs connected with rigid tubing of different diameters. He built an analogy of the pump to an electrical circuit, as diagrammed in figure 1.6. Using this analogy, he was able to make a prediction of the net flow rate as a function of the compression frequency. This electrical analogy is only applicable to the modifications that Moser made in defining the impedance pump and is not extendible to the single tube pump. His system required a closed loop system and, once again, the results were not compared with any experimental data.

The physical model that Moser used to create his theory once again requires a closed loop. If there was not a second distensible chamber, but rather two open ends,

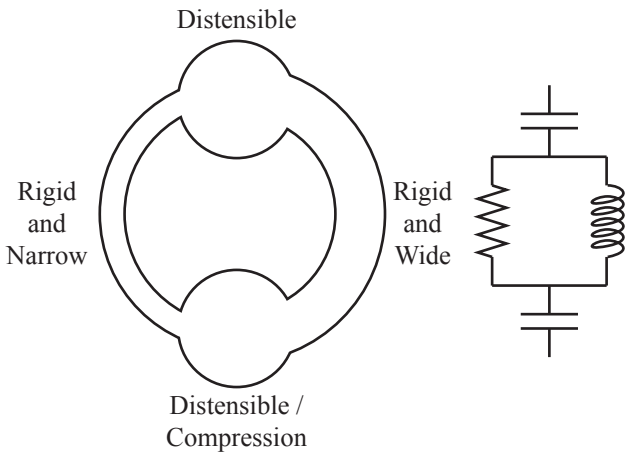

Figure 1.6: Moser's model of the impedance pump

his electrical circuit analogy would fail to predict a net flow. In addition, his plot of expected net flow at varying frequencies does not contain any distinct peaks or valleys that are characteristic of the pump's behavior as will be shown later.

Eunok Jung, in 1999, published her thesis on numerical simulations of a valveless pump using the immersed boundary method [13–15]. Her work consisted of a two-dimensional, computational model with a straight elastic section and a curved rigid section connecting the ends of the elastic pump (figure 1.7). The tube is filled with an incompressible, viscous fluid of constant density. It is compressed on the elastic section, off-center from the interfaces to the rigid section, in an oscillatory motion. Her results demonstrated that the direction and amplitude of the flow were dependent not only on the location of the compression but also on the frequency. Unfortunately, she made no physical model to describe the mechanism of the pump in her thesis.

One-dimensional simulations were carried out for a closed torus system [26] by Ottesen and an open system with two chambers at the end [2] by Borzi et al. The numerical models proposed by Borzi and Propst showed that an open loop system can create a net pressure head. Ottesen has been the only author to present quantitative experimental results. These results are limited to three data points, the net flow for one frequency at three pincher locations. Ottesen also presented qualitative results stating that the direction and mean flow is dependent on frequency and compression

Figure 1.7: Jung's model of the impedance pump

motion. Increased elasticity generally increased net flow. Also, as the position of the pinchers approaches the symmetric position, the net flow decreases.

1.3 The Impedance Pump Problem

Each of the previous works took a different approach to understanding the impedance pump. Gerhart Liebau demonstrated valveless pumping experimentally, showing that a single tube pumped rhythmically, can pump against a pressure head in an open loop. Subsequent papers focused on computational and analytical models to describe the phenomena. The lack of experimental data has been a weak point in the development of a model for impedance pumping. It has prompted theoretical and computational researchers to speculate on the parameters that are dominant in the function of the impedance pump. Our prior efforts [8] and those outlined in this thesis hopefully fill that void.

We can revisit the larger task of identifying the underlying physics that drives the impedance pump by answering a series of key questions through experimental observation.

- What features are necessary and sufficient to create an impedance pump?
- What parameters dominate the response characteristics of the pump?
- What effect do these parameters have?
- What features are inherent versus auxiliary to the pump's response?

- What is the mechanism that induces a net flow?

The answers to these questions will hopefully lead to the broader knowledge of how we can predict the behavior of an impedance pump and how we can design such a pump.

Chapter 2

Experimental Methods and Materials

Prior efforts have focused on analytical and computational approaches to explaining valveless pumping. With limited experimental data, the studies prior to this work hoped to predict the flow behavior of an impedance pump system. For this thesis, an experimental approach was chosen such that the pump's behavior could be explicitly measured prior to creating a model. Specific goals for the experiments included cataloging the pump's bulk behavior under a large range of parameters in order to identify those that are principal in the pump's performance and their effects. Further experiments were conducted to examine the pump's internal behavior including flow, pressure, and wall motion in time.

2.1 Experimental Flow Loop

A flow loop was constructed to test the impedance pump (figure 2.1). In its design, considerations were made to accommodate assorted tube geometries including changes in length, diameter, and thickness. This was accomplished using an interchangeable test section. It can hold horizontally an elastic tube of up to 6 inches in length and 3/4 inches in diameter. An additional 3 inches of length on each side are available for the tubing of mismatched impedance. The inlet and outlet flow rates, as well as the inlet and outlet pressures can be measured at this location. Two reservoirs are located at either end of the test section. An additional rigid tube connects the

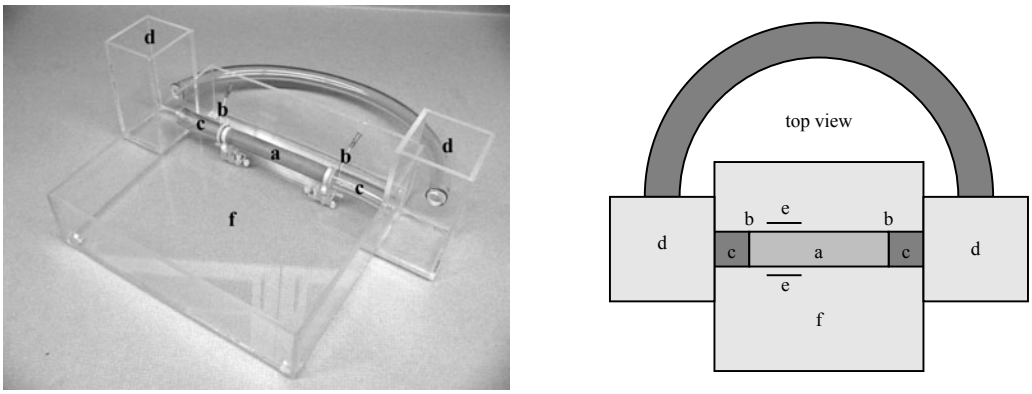

(a) (b)

Figure 2.1: Experimental Flow Loop: a - elastic section, b - pressure ports, c- flow measurement location, d - reservoirs, e - pinchers, f - secondary reservoir.

reservoirs creating a closed loop. This connection can be modified to adjust the resistance to the flow or be removed completely to create an open loop setup. The reservoirs have two purposes: to reduce the momentum of the flow exiting the pump such that the flow through the connecting loop is pressure driven, and to allow the system to be pressurized to different values with respect to the external pressure on the pliant section. A secondary reservoir surrounds the test section. Filling this allows ultrasound imaging of wall motion in both radial and axial slices.

2.2 Tubing Materials

Both elastic and inelastic tubing was tested. The elastic tubing used for the experiment was an amber latex tube, 1/32 inch in thickness with varying length. It has a tensile strength of 3500 PSI and a Shore A hardness rating of 35. The inelastic tubing used was a polyethylene tube, 3/4 inch in inner diameter, approximately 2 x 10^{-3} inches in thickness and 6 inches in length. In all cases, the ends were connected to a Tygon S50-L tubing 3/4 inch in inner diameter and 1/8 inch in thickness. The size scale and materials were chosen to be readily imaged by an ultrasound machine, which permits imaging of the flexible tube wall motion and flow profile within the tube while pumping.

2.3 Compression Mechanism

There was no mechanism readily available to pinch the tube in a prescribed manner. Ideally, the compression mechanism would be capable of a fully controllable compression profile including variable amplitude, frequency, and duty cycle. However, physical limitations in force require compromise of such qualities as amplitude and frequency.

2.3.1 Motorized

A device was constructed that relied on a motor to turn two geared wheels (figure 2.2). These wheels each have a pin on them that slides in a groove on the pinchers, creating a sinusoidal motion. It had been the intention to use a servo or stepper motor to control the pinchers. However, it became apparent that a motor could not provide a controlled motion at frequencies of interest. The pinchers followed a sinusoidal motion with a 1 inch diameter each. A maximum pinching frequency of 8 Hz was achievable with no further control over waveform of the compression.

2.3.2 Solenoid Activated

A second compression mechanism was built utilizing a solenoid (figure 2.3). The solenoid directly activated one pincher while another was mechanically linked to pinch from the other side of the tube. Though full control over the pinching profile was still not possible, this design allowed for variation in frequency, duty cycle, and amplitude with the use of a blockage. The duty cycle is defined as the fraction of the compression period during which the solenoid is active corresponding to an open tube. A maximum pinching frequency of 10 Hz and a duty cycle as short as 5% with complete closure from 3/4 inches was achieved.

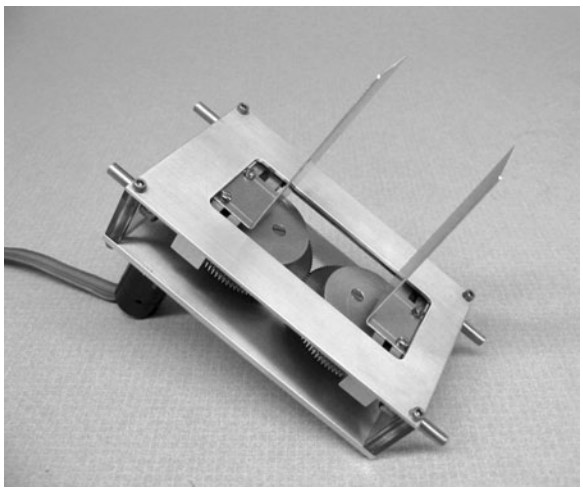

(a) Compression mechanism

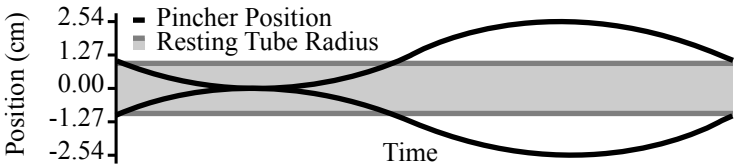

(b) Compression profile in time

Figure 2.2: Motorized compression mechanism and path

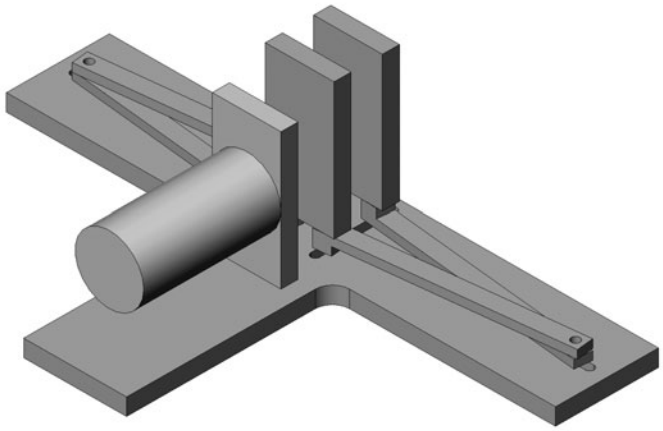

Figure 2.3: Solenoid activated compression mechanism

2.4 Measurement

The acquired data consisted of pressure and bulk flow measurements at the ends of the pliant tube. Additionally, ultrasound images were concurrently taken to capture the motion of the tube walls and fluid within the tube. The data were acquired using a National Instruments (Austin, TX) PCI-6035E data acquisition board.

2.4.1 Material Properties

Measurement of the compliance of the elastic tube was performed by filling an isolated section of tubing with different volumes and measuring the change in transmural pressure [31]. We selected a normalized definition of the compliance C as a function of cross-sectional area A, transmural pressure P, and cross-sectional area at rest of A_0. The change in diameter was inferred by assuming uniform expansion of the tube based on the volume added:

$$C = \frac{\partial A / \partial P}{A_0}$$

2.4.2 Pressure

Two diaphragm pressure transducers, Sensotec (Columbus, OH) 060-E067-02, were used to measure the pressure in time at both ends of the pliant section. The transducers have a range of 5 PSI, and an accuracy of 0.1%. They were connected to the system via a long semi-rigid tube. To verify that the connection does not interfere with the pressure reaching the transducer, we can calculate the natural frequency, damping ratio, attenuation and phase shift of the connecting system based on the equations presented by Holman [10].

Given the properties in table 2.1, we find that for a pressure signal, P_0, with a frequency of ω the natural frequency of the measurement system, ω_n, is

$$\omega_n = \sqrt{\frac{3\pi r^2 c^2}{4LV}}$$

Property	Symbol	Value
Volume of reservoir at pressure transducer	V	10^{-6} m^3
Length of tube	L	0.5 m
Radius or tube	r	0.001 m
Density of transmitting fluid	ρ	1000 kg/m^3
Speed of Sound in fluid	c	1500 m/s
Dynamic (absolute) viscosity	μ	10^{-3} kg/(m s)

Table 2.1: Parameter Values for Computing Pressure Transducer Dynamic Response

The damping ratio, h, is defined as

$$h = \frac{2\mu}{\rho c r^3}\sqrt{\frac{3LV}{\pi}}$$

The attenuation, defined as the absolute value of the pressure measured by the sensor, P, divided by the pressure signal, P_0, is

$$\left|\frac{P}{P_0}\right| = \frac{1}{\left(\left(1-\left(\frac{\omega}{\omega_n}\right)^2\right)^2 + 4h^2\left(\frac{\omega}{\omega_n}\right)^2\right)^{1/2}}$$

And the phase shift, Φ, in the pressure signal, P_0, and pressure measured, P, is

$$\Phi = \tan^{-1}\frac{-2h\left(\frac{\omega}{\omega_n}\right)}{1-\left(\frac{\omega}{\omega_n}\right)^2}$$

The natural frequency is approximately 3300 Hz, corresponding to negligible damping, attenuation, and phase shift at the frequencies we interested are in.

2.4.3 Flow

A Transonic (Ithaca, NY) HD01 flow meter system is used to measure the dynamic flow rate. It has a sample rate of 0.9 MHz, range of ± 50 L/min, and a resolution of .025 L/min. The sampling frequency far exceeded the needs of the experiments. The meter functions using Doppler ultrasound with a cuff around a calibrated tubing material. In the case of this study the materials are Tygon R-3603 and Tygon S50-L.

The probe was placed just past the ends of the primary pliant section.

2.4.4 Ultrasound Imaging

Ultrasound allowed for the high speed imaging of the tube wall for various slices. Provided that the flow was seeded with particles, it is also capable of capturing the fluid motion. The ultrasound machine available to the project was a General Electric (GE) Vingmed System FiVe. It is equipped with three different probes:

- The FPA 10 MHz 2A is a pediatric cardiac probe capable of acquiring data at frame rates up to 297 frames per second. It has a depth resolution of 0.015464 cm and 0.011001 rad. The maximum depth of penetration is 14 cm. The frame rate is dependent on the width and depth of the measurement.

- The FPA 2.5 MHz 1C is an adult cardiac probe capable of acquiring data at frame rates of up to 212 frames per second. The maximum depth of penetration is 30 cm. The frame rate is dependent on the width and depth of the measurement.

- The FLA 10 MHz 1A KZ314118A is a linear phase array probe that is capable of acquiring data at frame rates of approximately 17 frames per second. This probe has the highest spatial resolution but the frame rate is significantly lower than that of the other two probes.

The pediatric probe is the most suitable for the project because of its spatial and temporal resolution.

Ultrasound imaging was used for the measurement of wave speed on the surface of the tube. To accomplish this, the secondary reservoir was filled with water. An ultrasound probe was placed in the water to image axial slices of the tube. The edges of the axial slices were outlined and the cross-sectional width was measured along the length of the tube. By determining the positional shift of the cross-sectional width at a known frame rate, the wave speed was determined.

To determine the natural frequency response and behavior of the impedance system a single waveform response was measured. The system was pinched once 1 inch from one end of the tube with a profile equivalent to that of pinching at a frequency of 4.7 Hz. Pressure, flow, and ultrasound images were simultaneously acquired.

Chapter 3

Experimental Results

3.1 Basic Systemic Behaviors

The basic systemic behaviors of the experimental setup were first measured to characterize its properties. Included are the compliance of the primary latex tubing used in the experiments and the wave speed on the surface of the elastic tube when filled with water to a fixed pressure.

3.1.1 Compliance

The compliance of the elastic tube used was measured by the method outlined in section 2.4.1 to be constant at 0.002525 mm Hg^{-1} within the pressure ranges observed during operation (figure 3.1). The maximum change in cross-sectional area due to elastic expansion for this compliance was under 1% suggesting that elastic forces are not essential to the pumping mechanism.

3.1.2 Wave Speed

For one typical configuration, the average wave speed observed on the surface of the tube was approximately 59 cm/sec when pressurized with water to 2.8 mm Hg (figure 3.2). In response to a single compression, the tube resonated at integer multiples of 8.8 Hz. This frequency is equivalent to the rate at which a single wave would travel half the length of the elastic tube at 59 cm/sec. However, the wave speed is

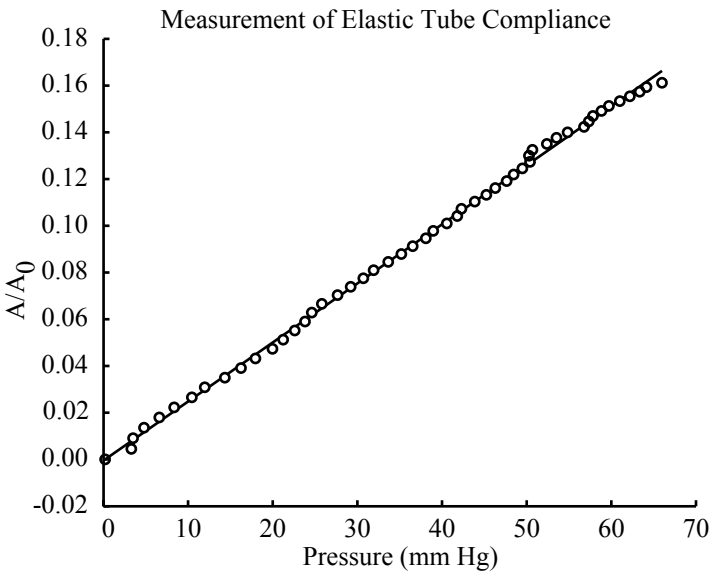

Figure 3.1: Measured compliance of amber latex tube 3/4 inch in inner diameter, 1/32 inch in thickness, with a tensile strength of 3500 PSI and a Shore A hardness rating of 35.

unique to each data set. When the tube is attached to the flow loop, the tension and other factors affecting the wave speed, and consequently the resonant frequency, are modified.

3.1.3 Reservoir Natural Resonant Frequency

In an effort to separate the behavior of the impedance pump with that of the flow loop including the reservoirs, the natural frequencies associated with the reservoirs and flow loop were measured with the pump removed. In its place was a short rigid tube of the same diameter. The reservoirs and adjoining tubing were filled to the same height used in all the experiments except for those where the height was deliberately changed to increase the transmural pressure across the elastic section. The setup was then lifted and quickly lowered to create an imbalance in the fluid level between the two reservoirs. The flow rate was subsequently measured through the short tube section whenever the short section was not occluded and through the long section when the short section was occluded. A Fourier transform of the resulting data

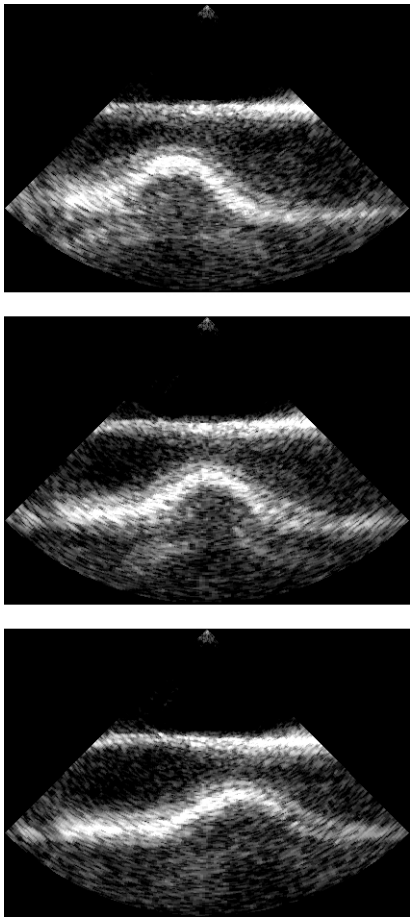

Figure 3.2: Ultrasound images of an axial slice of an elastic tube demonstrating wave motion used in the calculation of wave speed.

indicated the system, in this configuration, behaved as a simple harmonic oscillator with a resonant frequency of 0.300 Hz when allowed to flow through both the short rigid section and the long rigid section, 0.167 Hz when allowed to flow only through the long rigid section, and 0.234 Hz when allowed to flow only through the short rigid section.

3.2 Intrinsic Behaviors

The impedance pump is a remarkably robust system in its design. For every configuration we have built to date, an appropriate frequency has been found to drive significant net flow. Though the specific response of each configuration can be quite different, there are behaviors intrinsic to the impedance pump that can be observed in all configurations. In all cases, flow rates are considered positive when flowing from the short end to the long end of the elastic section.

3.2.1 Wall Motion

Imaging of the sectional slices of the impedance pump show the wave propagation along the length of the tube and reflection at the end. Also visible is that the tube is not expanding in diameter but rather functioning as a pliant tube that can buckle. This is because the pressures created in the system are not sufficiently high enough, given the compliance of the material used, to stretch the material beyond 1% of its resting diameter, as anticipated by the compliance measurement. This phenomenon is further discussed in section 3.2.5.

The configuration shown in figures 3.3 and 3.4 was a 6 inch long latex tube compressed with the motorized pinchers at 1 inch from the end. The compression is on the left of the images, at a frequency of 6.25 Hz. Cross-sectional slices were taken at 2, 3, 4, and 5 inches. One complete pinching cycle is shown. The pinchers remain in contact with the tubing material during the compression phase. As they begin to retract, the pinchers lose contact with the tubing and the ensuing tube motion is independent of the pincher motion. In the optimized case, we can see that the

frequency of compression is matched with the frequency of refilling of the tube at the site of the compression such that just as the tube begins to relax following its refilling the pinchers begin to compress the tube again. This suggests that the impedance pump relies on resonance to build pressure and flow.

3.2.2 Role of Resonance

What role does resonance play in frequency response of an impedance pump? We first look at the flow response to an impulse and the corresponding fast Fourier transform (FFT) (figure 3.5). To do so, the solenoid pinchers were used on a 6 inch length of latex tubing. At first glance, the time response resembles a simple damped harmonic oscillator as does the envelope around the FFT. However, the FFT shows us that there are multiple frequency peaks within that envelope implying that the mechanics are of a more complex resonating system.

A look at the net flow rate as a function of frequency reveals that the resonant frequency of the system is also very near the frequency at which maximum positive net flow occurs. Maximum negative net flow occurs around the first multiple of the resonant frequency.

3.2.3 Transient Response

The resonant, pulsatile nature of the impedance pump leads us to ask about the transient nature of the pump. How long does it take to establish a net flow? Will the pump exhibit the same net flow when the forcing frequency is approached from different directions? Does the pump have different characteristics when approaching a negative net flow versus a positive net flow?

We look again at the data used to establish the resonant behavior of the impedance pump. This time, however, we inspect the development of the flow to reach a quasi-steady state. A comparison between the flow in time and the moving average of the flow in time are compared for each case: high positive net flow (figure 3.7), low positive net flow (figure 3.8), and high negative net flow (figure 3.9).

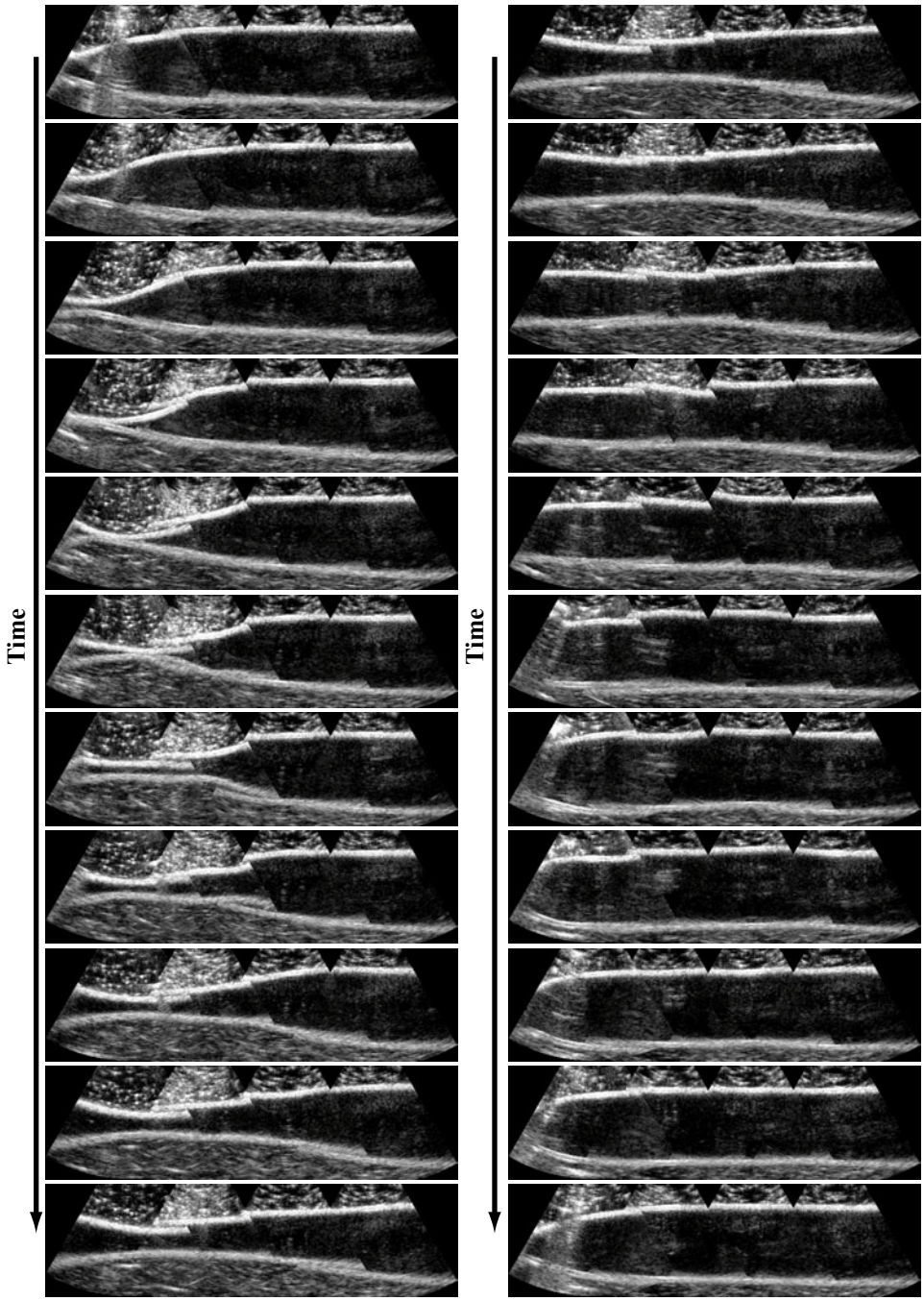

Figure 3.3: An axial section of impedance pump in time during highest net flow for a single compression cycle.

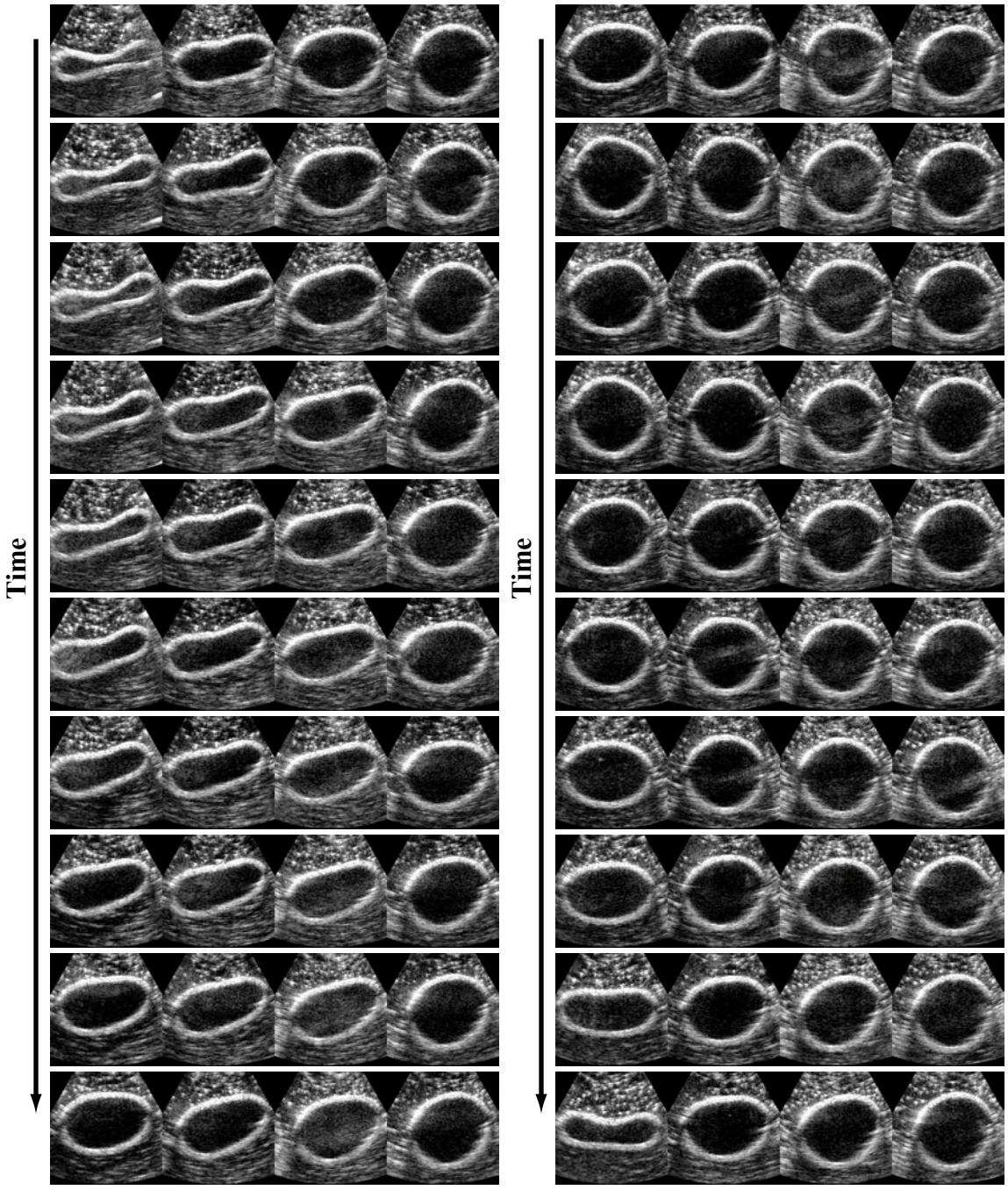

Figure 3.4: A cross section of impedance pump in time during highest net flow for a single compression cycle.

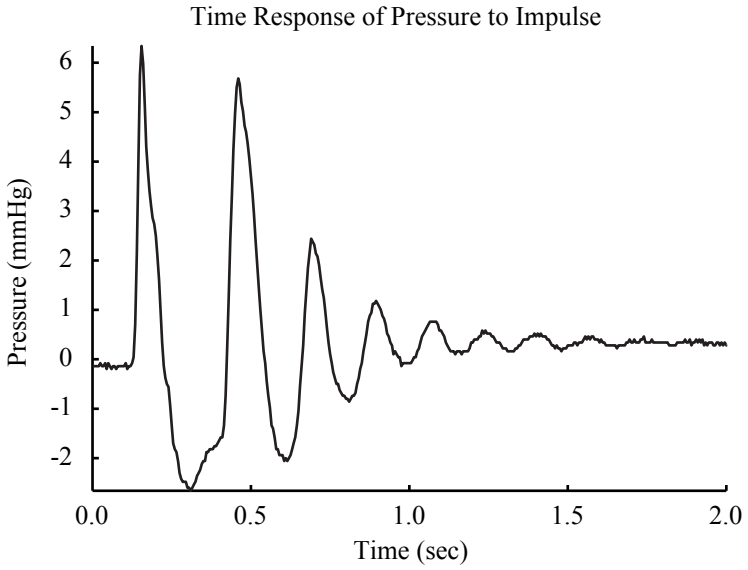

(a) Impulse response in time.

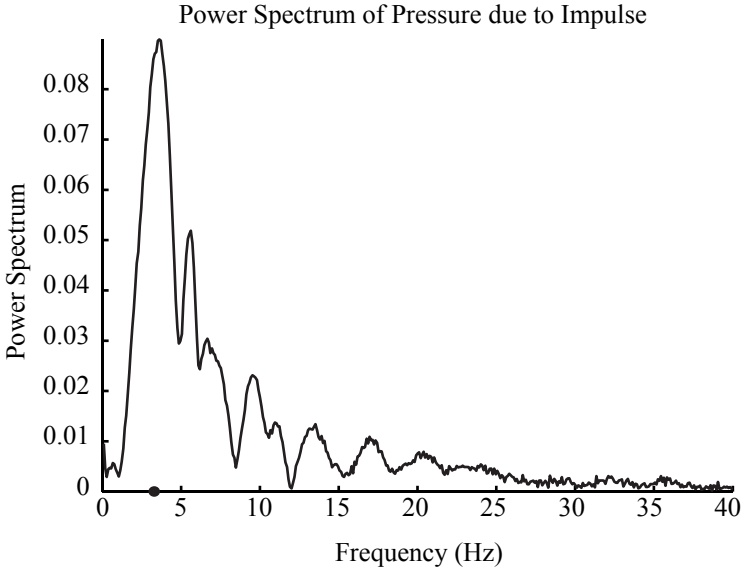

(b) Impulse response in frequency space and frequency of highest forward flow.

Figure 3.5: Response in time and frequency of pressure at exit interface to an impulse.

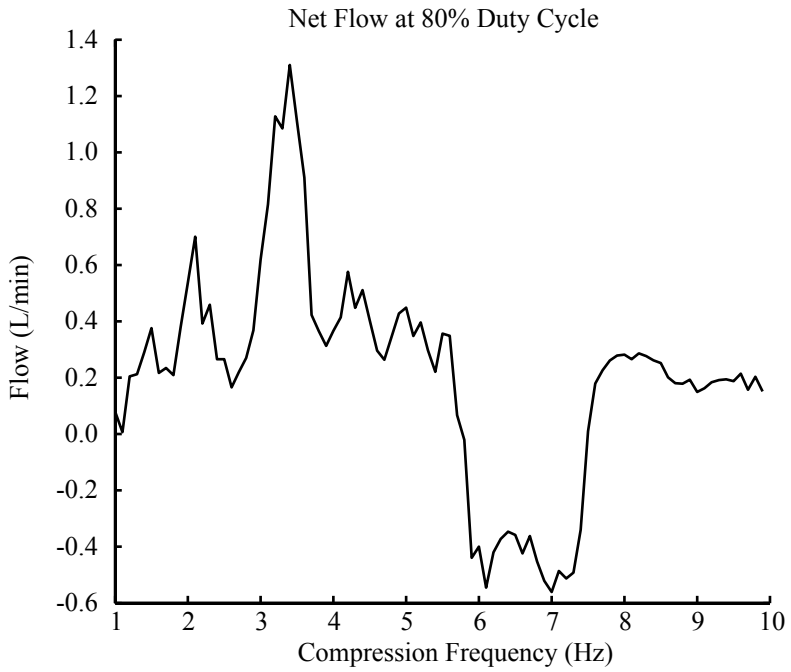

Figure 3.6: Sample mean flow as a function of frequency for a fixed configuration.

We find that for the high positive net flow case, an equilibrium is reached faster than for the low flow or negative flow cases.

3.2.4 Pressure and Flow Relationship

We examine the relationship between pressure and flow at one end of the pliant section for cases of high positive net flow, low positive net flow, and high negative net flow. During the highest positive net flow, the pressure and flow appear to be locked in phase (figure 3.10). This is a direct result of activating the resonant frequency of the system.

In the low flow and negative flow cases, the flow-pressure profile moves counter-clockwise in time (figures 3.11, 3.15). Just as the pressure drops, a flow forms filling in that area from a higher pressure region. The phase at which this occurs between the ends of the pliant tube can be coordinated in such a way as to select what the position of the higher pressure region should be, and in turn, inducing a unidirectional flow. This coordination is achieved by modifying the frequency and duty cycle. The same

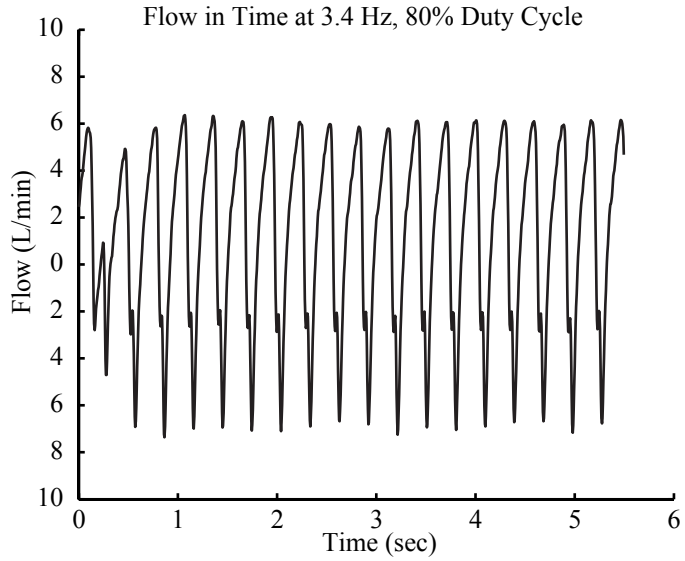

(a) Measured Flow

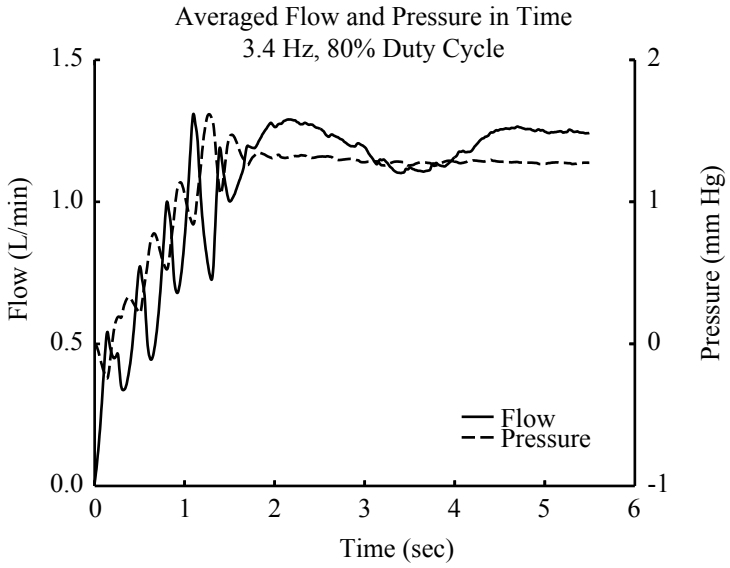

(b) Averaged Flow

Figure 3.7: Response of flow rate in time, both measured and averaged at highest mean flow rate.

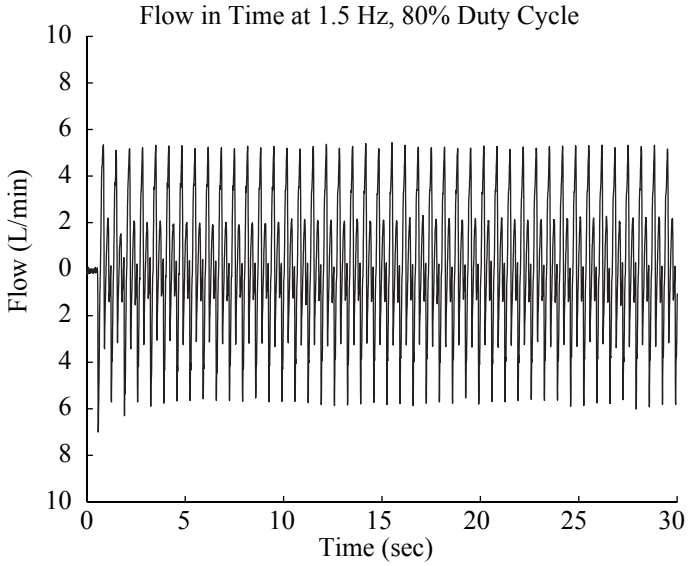

(a) Measured Flow

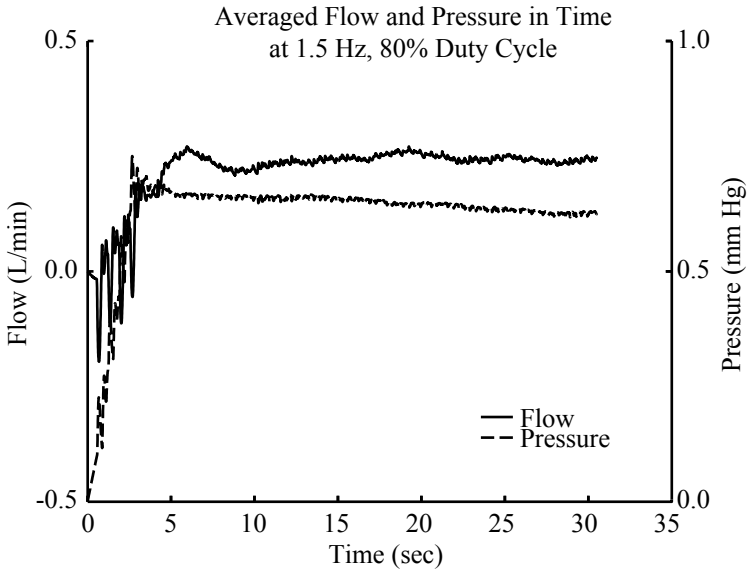

(b) Averaged Flow

Figure 3.8: Response of flow rate in time, both measured and averaged at low mean flow rate.

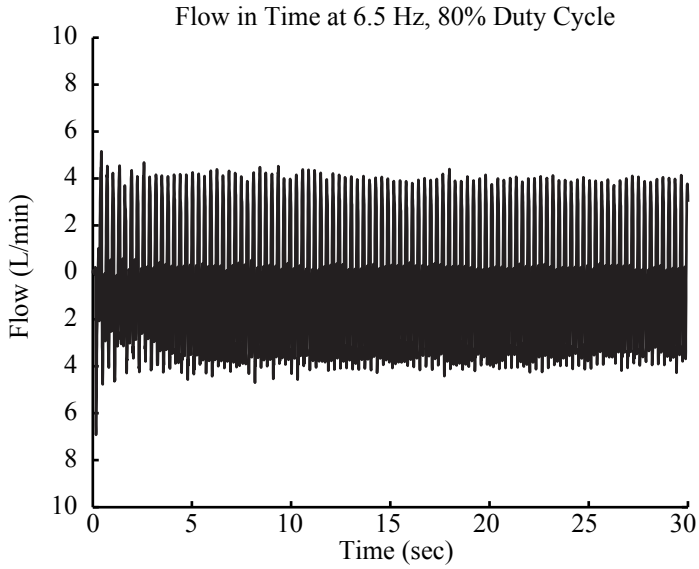

(a) Measured Flow

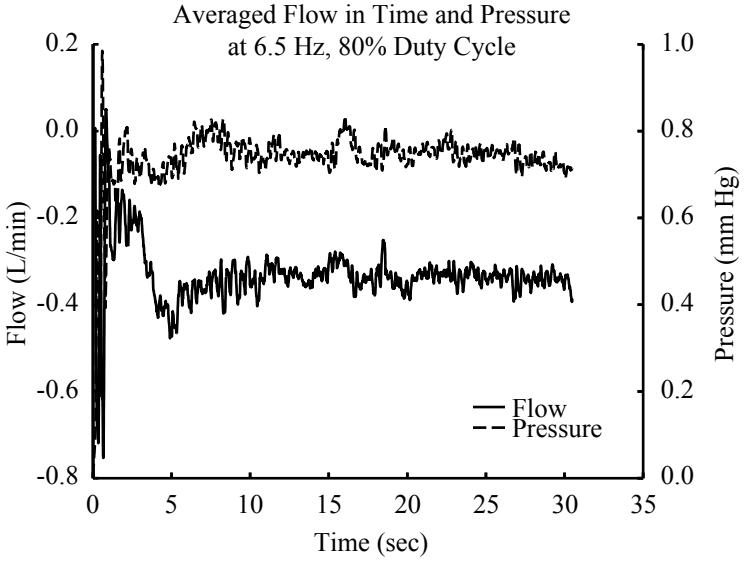

(b) Averaged Flow

Figure 3.9: Response of flow rate in time, both measured and averaged at high negative mean flow rate.

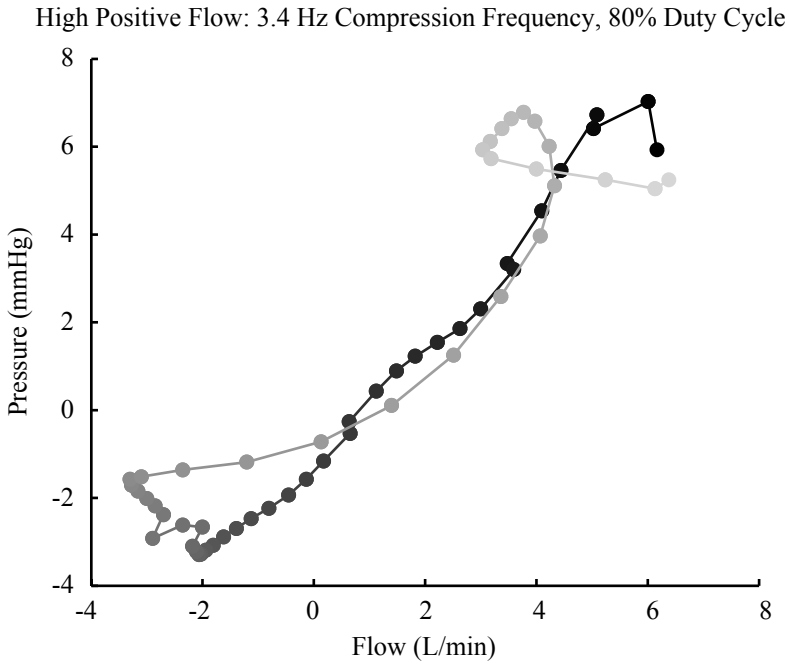

Figure 3.10: Pressure-flow relationship averaged over one compression cycle at end of long section during highest positive net flow. Points are equidistant in time. Color lightens forward in time.

phenomenon is observed when the flow is seeded in an axial slice ultrasound video. As the pressure decreases, the tube begins to collapse. When the traveling region of low pressure reaches the end it reflects off of the impedance mismatch causing the tube to open. Fluid immediately begins to fill in from behind the wave front. Once the section has expanded to its resting diameter, it begins to exert pressure back into the fluid. It reaches a critical threshold when the pressure differential can no longer drive the flow in the same direction and the flow reverses (figure 3.12).

We take a closer look at the pressure-flow profile for negative flow by comparing the results for many cycles (figure 3.13), phase-averaged with the compression frequency (figure 3.14) and finally phase-averaged by half the compression frequency (figure 3.15). Unlike the positive flow cases, both pressure and flow have periods double the duration of the compression period. However, this occurs at all higher compression frequencies and not only when the net flow is negative. Negative net flow, is caused by the same mechanism as forward flow. However, the frequency of compression is

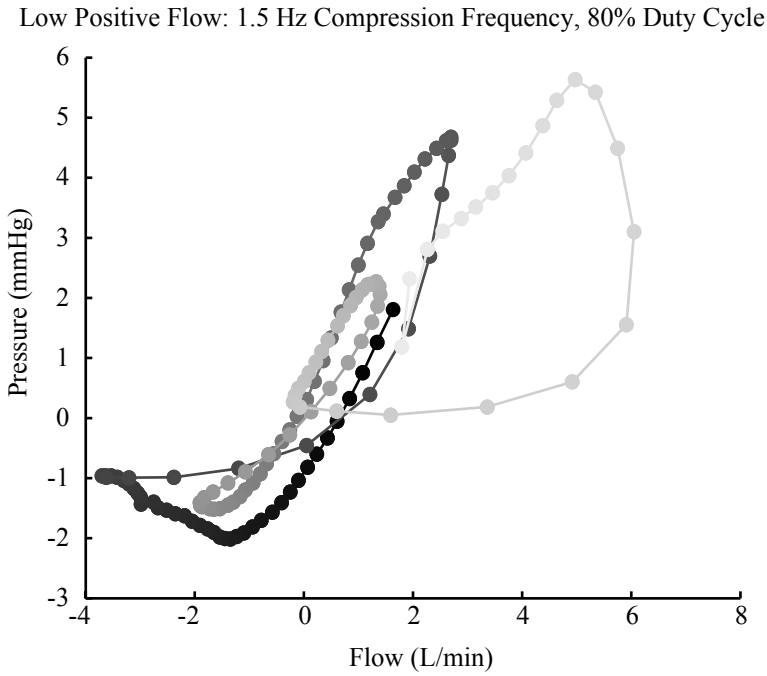

Figure 3.11: Pressure-flow relationship averaged over one compression cycle at end of long section during low positive net flow.

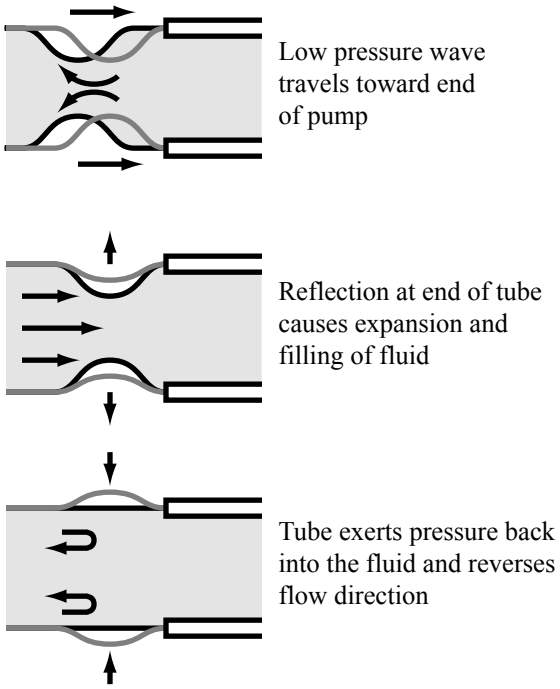

Figure 3.12: Illustration of pressure flow relationship near one end of the pliant tube.

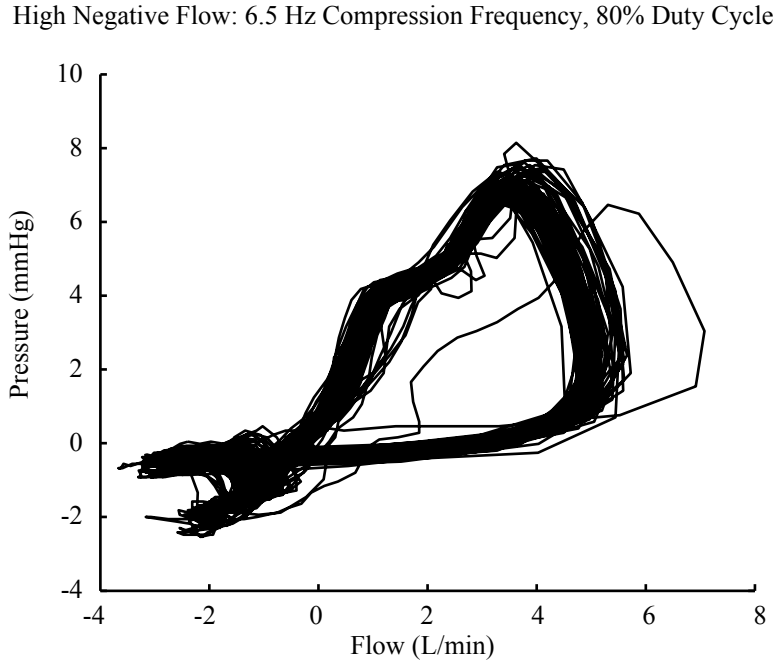

Figure 3.13: Pressure-flow relationship over all compression cycles at end of long section during high negative net flow.

such that the coordination between the pressures at the two ends of the pump result in a net negative flow.

3.2.5 Role of Elasticity

The compliance and range of pressures measured during the operation of the impedance pump show that the perimeter of the elastic latex tube used in the majority of the experiments did not expand past 1% of the resting perimeter whereas large changes in cross-sectional area were observed as the tube collapsed. To led us to evaluate the necessity of elasticity for the function of the impedance pump.

To test the hypothesis that elasticity is not required, experiments were conducted using a polyethylene, inelastic, pliant tube. When compressed manually at comparable frequencies to the previous trials, a net flow rate over 2 L/min was achieved, similar in magnitude to the elastic tube pinched under similar conditions. It follows that it is not the elastic properties of the tube that provide a restoring force to

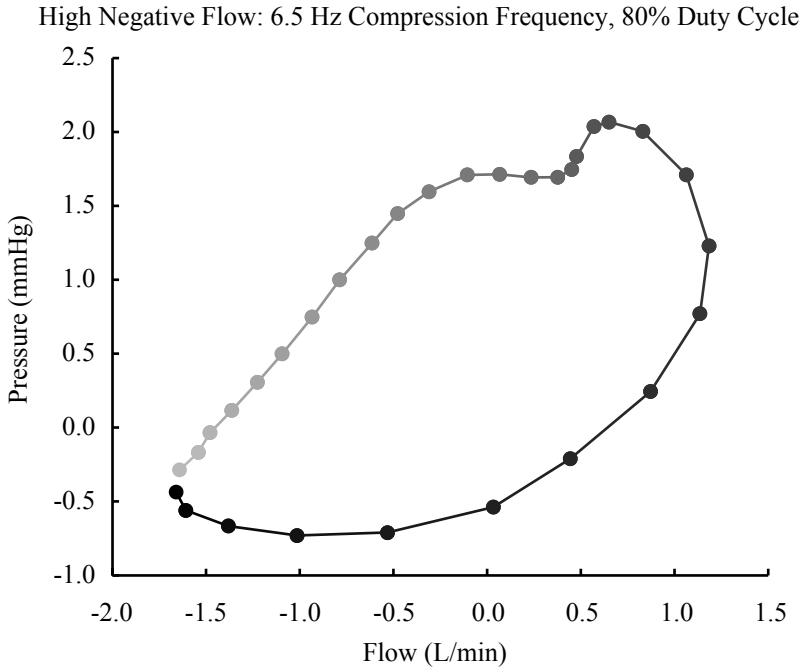

Figure 3.14: Pressure-flow relationship averaged over one compression cycle at end of long section during high negative net flow.

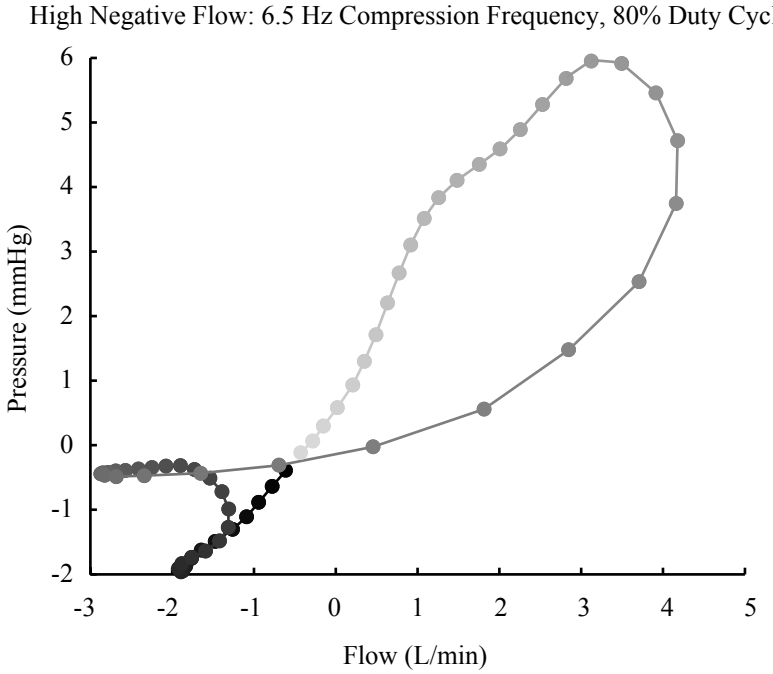

Figure 3.15: Pressure-flow relationship averaged over two compression cycles at end of long section during high negative net flow.

refill the tube and transmit waves but rather gravity that refills the tube from the reservoirs.

This expands the possible designs one might consider in the application of an impedance pump. In a neutrally pressurized environment elasticity may be used as the restoring force and the material would have to be chosen accordingly. However, for a pump loop that is naturally pressurized a wider range of materials and options are available. The arterial system, for example, is pressurized with respect to the body cavity. On a micro-scale, surface tension on a water droplet increases the pressure within the droplet with respect to the surrounding air. This pressure can also act as the restoring force for an impedance pump.

3.3 Bulk Flow Behaviors

3.3.1 Frequency and Position

To test how the origin of the compression affects the net flow rate as a function of frequency, a set of measurements was acquired for frequencies ranging between 1 and 8 Hz using the motorized pinchers system (figure 3.16(a)). The location of pinching spanned the full length of the elastic tube. In all cases, the tube was 5 3/4 inches long and the compression was 1 inch wide unless explicitly mentioned.

To properly compare the results of this experimental setup with others, especially on different scales, the data can be made dimensionless. First, the flow rate is normalized by half the volume displaced by the pinchers times the compression frequency as suggested by Thomann [32]. Because we are concerned with a pulsatile flow through a tube, the Womersley number, α, arises as a useful tool to make the frequency of compression non-dimensional. The Womersley number is defined as $\alpha = r\sqrt{\frac{\rho\omega}{\mu}}$ where r is the resting radius of the pump, ρ is the density of the fluid being pumped, ω is the compression frequency, and μ is the dynamic (absolute) viscosity. The location of the pincher is measured as a percentage of the distance from one end of the elastic section to the center of the pincher width compared to the total length of the elastic

section (figure 3.16(b)).

The net flow rate as a function of the non-dimensional pinching frequency, the Womersley number, maintains a similar trend between different pincher locations. In this trend we see a series of distinct peaks at which flow maxima occur. All the flow rates have been non-dimensionalized by half the rate of volume displaced by the compression. The unique frequency dependence of the net flow rate implies the occurrence of resonance, a consequence of wave propagation and reflection due to impedance mismatching. As the position of the pincher location moves toward the center of the primary elastic section, the location of those peaks shifts to slightly lower frequencies. Assuming a constant wave speed, these observations further our hypothesis of interfering waveforms, since an increase in the distance of the compression from one end increases the time necessary for a wave to travel that distance and back to the pincher location. This would result in a downshift of the frequency response. The magnitude of the net flow also decreases to zero as the pincher moves toward and becomes symmetric about the center. Increasing the distance of the compression from the ends further attenuates the wave, decreasing the pumping energy and flow rate. When the compression is in the center, the system is fully symmetric and no flow is expected. The highest non-dimensional net flow rate of 2.62 occurring at a Womersley number of 21.7 (4.7 Hz) exceeds the volumetric rate of fluid displaced by the compression. A peristaltic system non-dimensionalized in the same manner would result in a constant non-dimensional flow rate of 2. As a first approximation, this demonstrates that the impedance pump can be more efficient than a peristaltic system and is further discussed in section 3.3.7.

Flow rates as a function of time were further investigated at select Womersley numbers based on the net flow rates found in the trials (figure 3.17(a)). Womersley numbers of 16.4 (2.7 Hz), 19.7 (3.9 Hz), 21.7 (4.7 Hz), and 25.7 (7.1 Hz) compressed at a distance of 1 inch were chosen to compare the flow profiles at resonant peaks with a non-resonant flow profile. In all cases, significant backflow was observed. However, the non-resonant case had a longer semi-steady period of backflow whereas the resonant cases immediately began to accelerate forward after reaching their respective negative

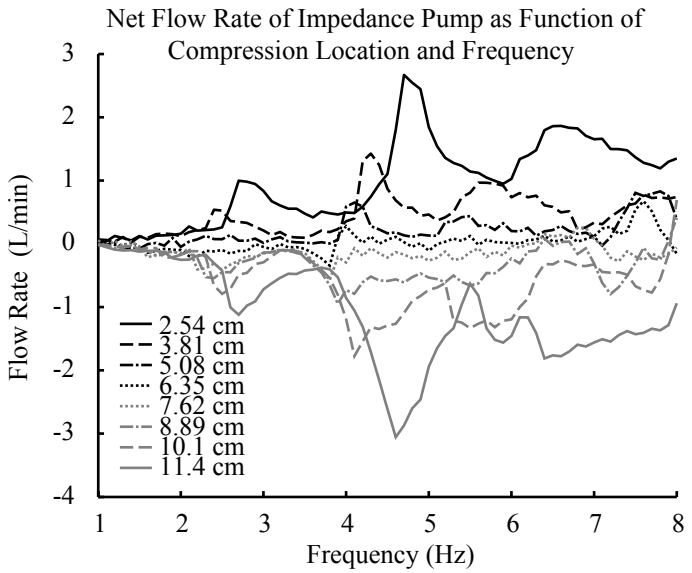

(a) Dimensional

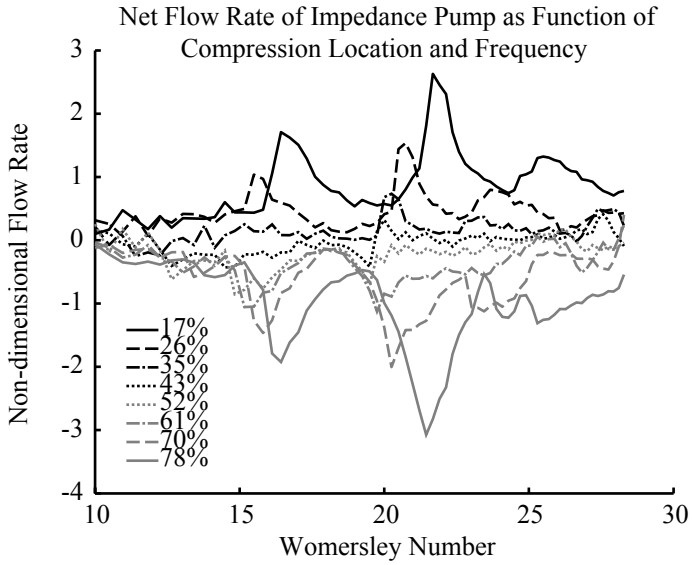

(b) Dimensionless

Figure 3.16: The net flow rate of the impedance pump as a function of compression position and frequency.

peaks. An FFT of the flow waveform has peaks at the forcing frequency plus an integer multiple of an unknown frequency that may be related to the natural frequency of the elastic section (figure 3.17(b)). What is interesting to notice is that the tallest FFT peak occurs at the same frequency as the highest net flow rate and the remaining FFT peaks decay in amplitude around the tallest. This further supports our hypothesis of resonating waves within an impedance chamber. By determining the resonant frequency of an impedance system, one may be able to predict the subsequent pump behavior under various compression profiles.

3.3.2 Frequency and Transmural Pressure

The experiment was repeated varying transmural pressure at rest across the wall of the elastic section with the pincher located at a constant position of 1 inch. Figure 3.18 shows that by increasing the internal pressure of the system, the peak net flow rate decreases and the frequency response shifted to higher values. One would expect this result from a shift in wave speed. This phenomenon is exaggerated by the method for non-dimensionalizing the net flow rate.

3.3.3 Frequency and Compression Width

To modulate the amount of energy imparted into the fluid, the experiment was repeated for varying pincher widths. In absolute terms, a wider pincher corresponds to a larger volume being displaced and therefore more energy being imparted into the fluid, and to higher flow rates (figure 3.19(a)). However, when non-dimensionalized against the rate of volume displacement by the compression, no clear pattern emerges (figure 3.19(b)). As the width of the compression approaches the distance from the end of the elastic section, other behaviors will begin to dominate. No longer is just the volume displaced changing, but also the distance the waves travel from the pincher to the end of the elastic section and back. Flow reversal is also observed when the pincher width is narrowed to 4.3% and 8.7% of the total length of the elastic tube. The magnitude of the reversed flow in this case is significantly lower than the forward

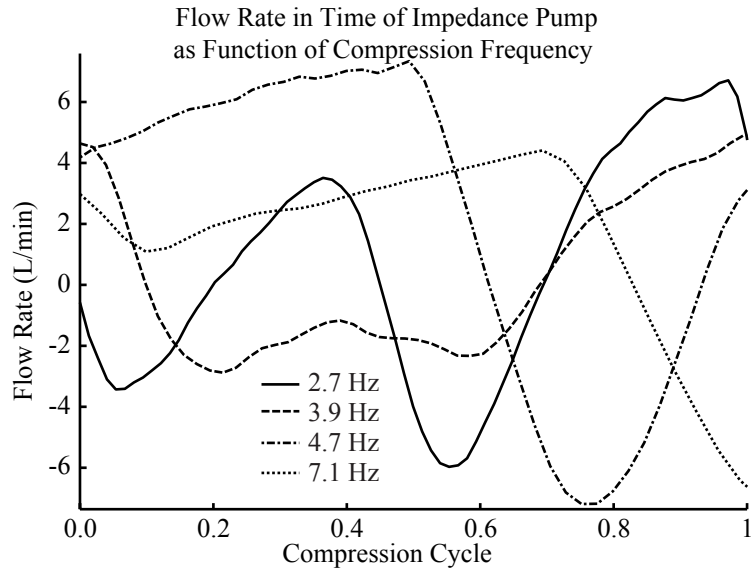

(a) Flow Rate

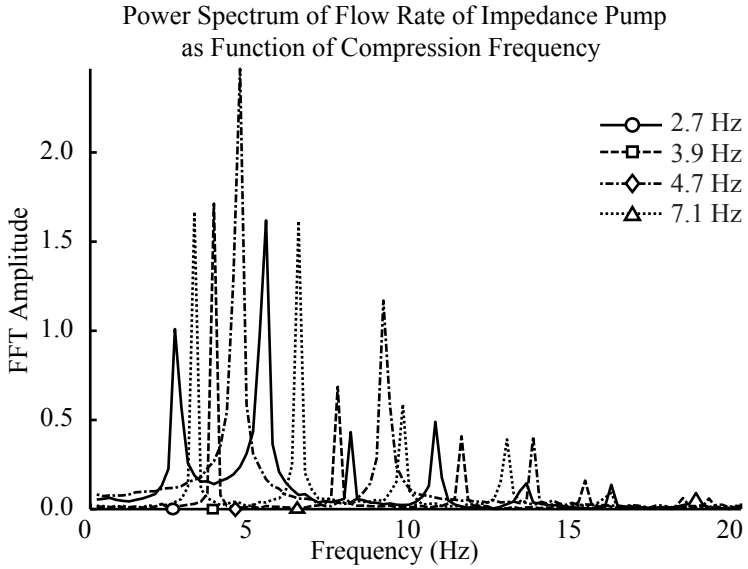

(b) FFT of Flow Rate

Figure 3.17: The flow rate in time and its Fourier transform for selected compression frequencies.

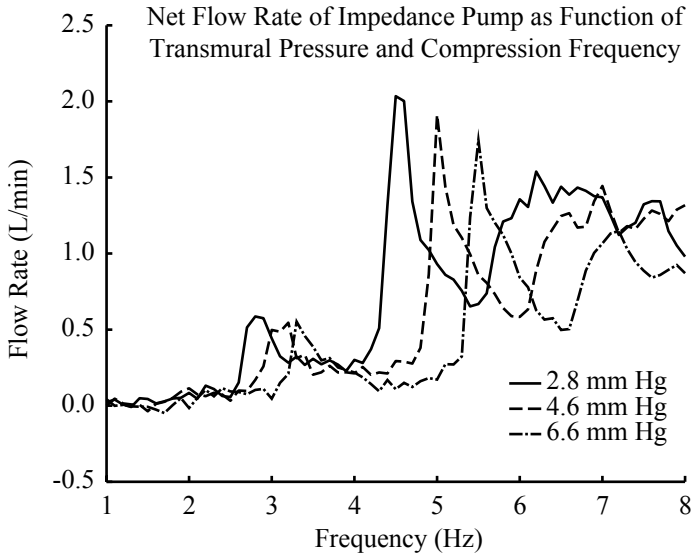

(a) Dimensional

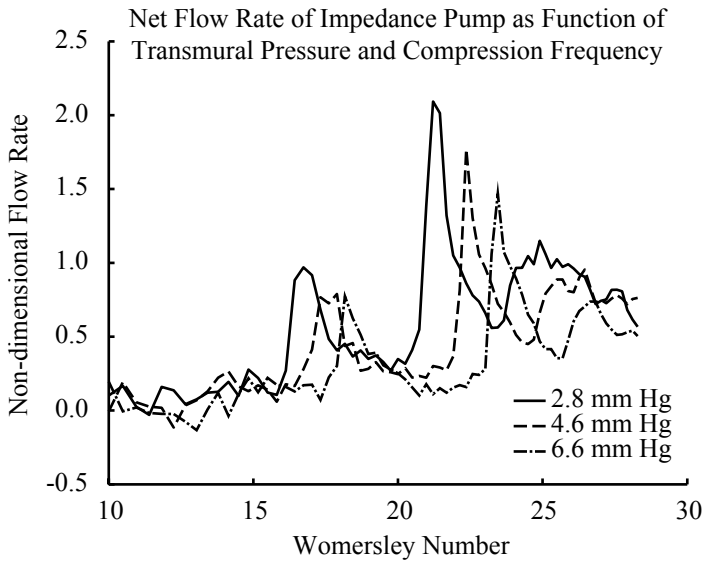

(b) Non-dimensional

Figure 3.18: The net flow rate of the impedance pump as a function of transmural pressure and compression frequency.

direction.

3.3.4 Frequency and Systemic Resistance

The resistance to flow of the system was also adjusted far from the elastic section by applying a constriction of varying diameter (figures 3.20, 3.21). As the resistance went up, the flow rate went down, and the pressure head went up as is typical in a pump. The pressure head as a function of frequency maintained a similar profile to the flow rate as a function of frequency with the peaks in pressure occurring at the same frequencies as the peaks in net flow rate. The power converted toward pumping the fluid therefore also has this non-linear profile.

3.3.5 Frequency and Viscosity

The effects of viscosity on the performance of the impedance pump were tested by preparing glycerol solutions with different fractions of glycerol to water. The solutions tested were 0%, 12%, 23%, 32%, and 47% glycerol by mass corresponding to relative viscosities of 1.0 cP, 1.3 cP, 1.8 cP, 2.4 cP, and 4.6 cP respectively. The resulting frequency response curve (figure 3.22(a)) shows little change for different viscosities. The non-dimensionalized response curve (figure 3.22(b)) on the other hand, shows peaks at dramatically different locations because the Womersley number incorporates the relative viscosity. These results demonstrate that the resonance phenomena is unaffected by relative viscosity within this range. It would seem, that the wave speed also remains unaffected.

3.3.6 Frequency and Duty Cycle

To study the effect of duty cycle, the solenoid-driven pinchers were used on a 6 inch long latex tube. A quantitative look was taken on the effects of duty cycle on the direction of the flow rate (figure 3.23). The duty cycle is defined in section 2.3.2 as the fraction of the compression period during which the solenoid is active corresponding to an open tube. When the duty cycle is modified, two things happen: the flow is

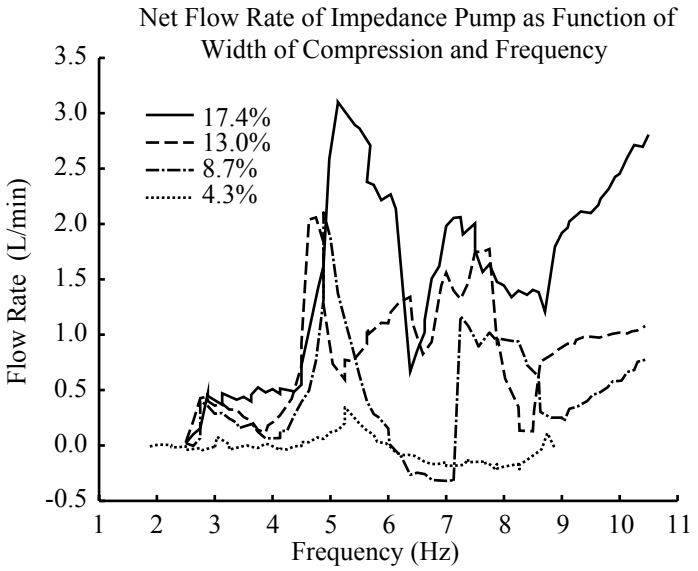

(a) Dimensional

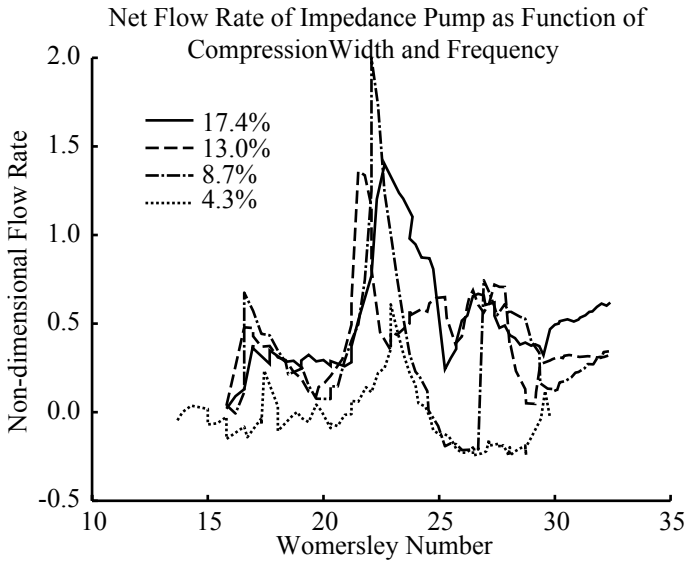

(b) Non-dimensional

Figure 3.19: The net flow rate of the impedance pump as a function of compression width represented as a fraction of the total length of the elastic section and frequency.

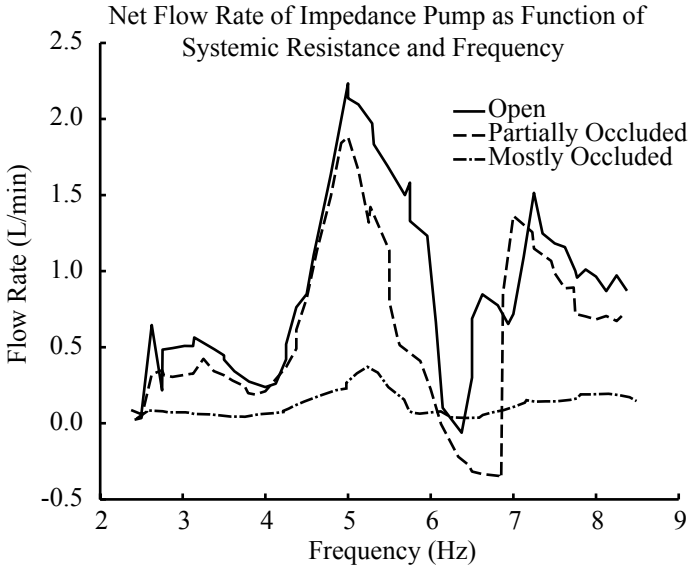

(a) Dimensional

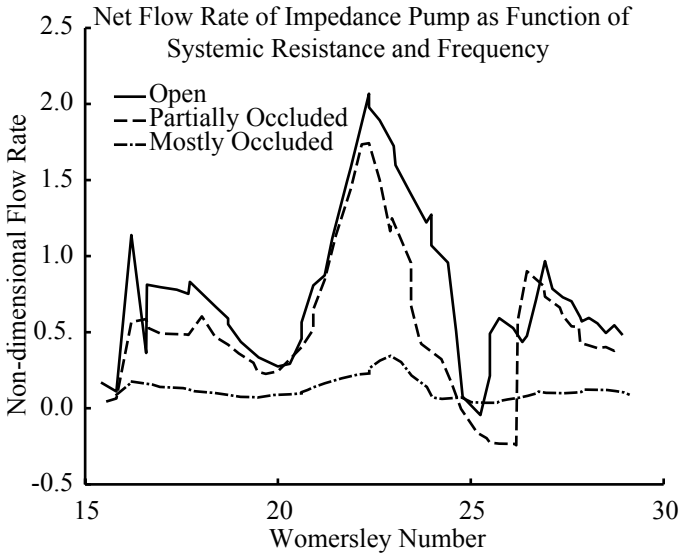

(b) Non-dimensional

Figure 3.20: The net flow rate of the impedance pump as a function of systemic resistance and compression frequency.

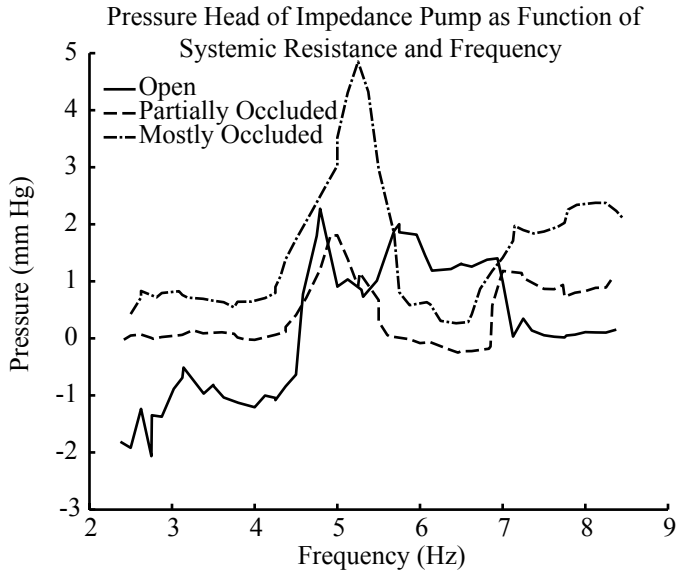

(a) Dimensional

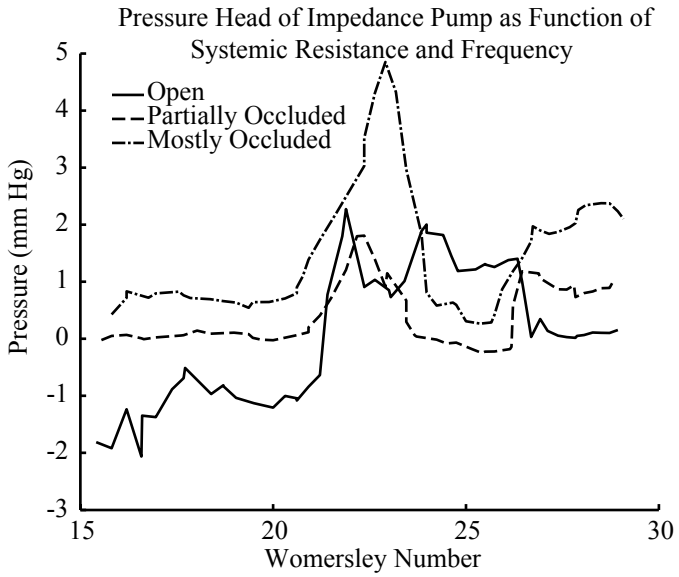

(b) Non-dimensional

Figure 3.21: The net pressure head of the impedance pump as a function of systemic resistance and compression frequency.

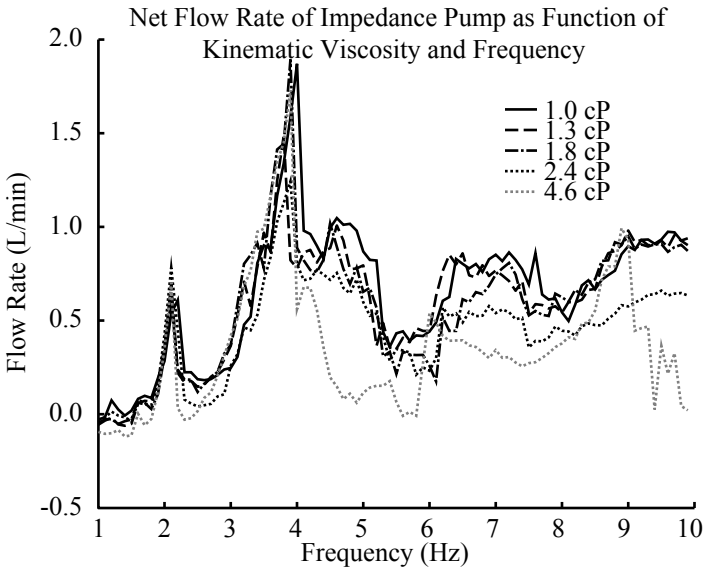

(a) Dimensional

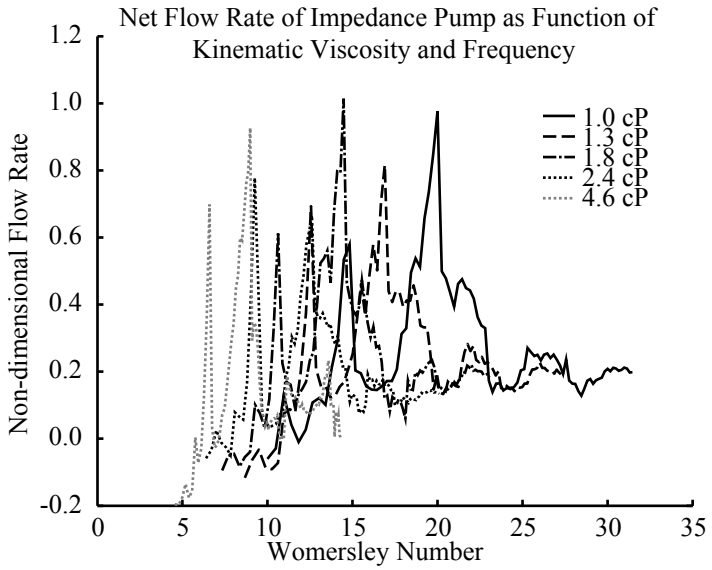

(b) Non-dimensional

Figure 3.22: The net flow rate of the impedance pump as a function of kinematic viscosity and compression frequency.

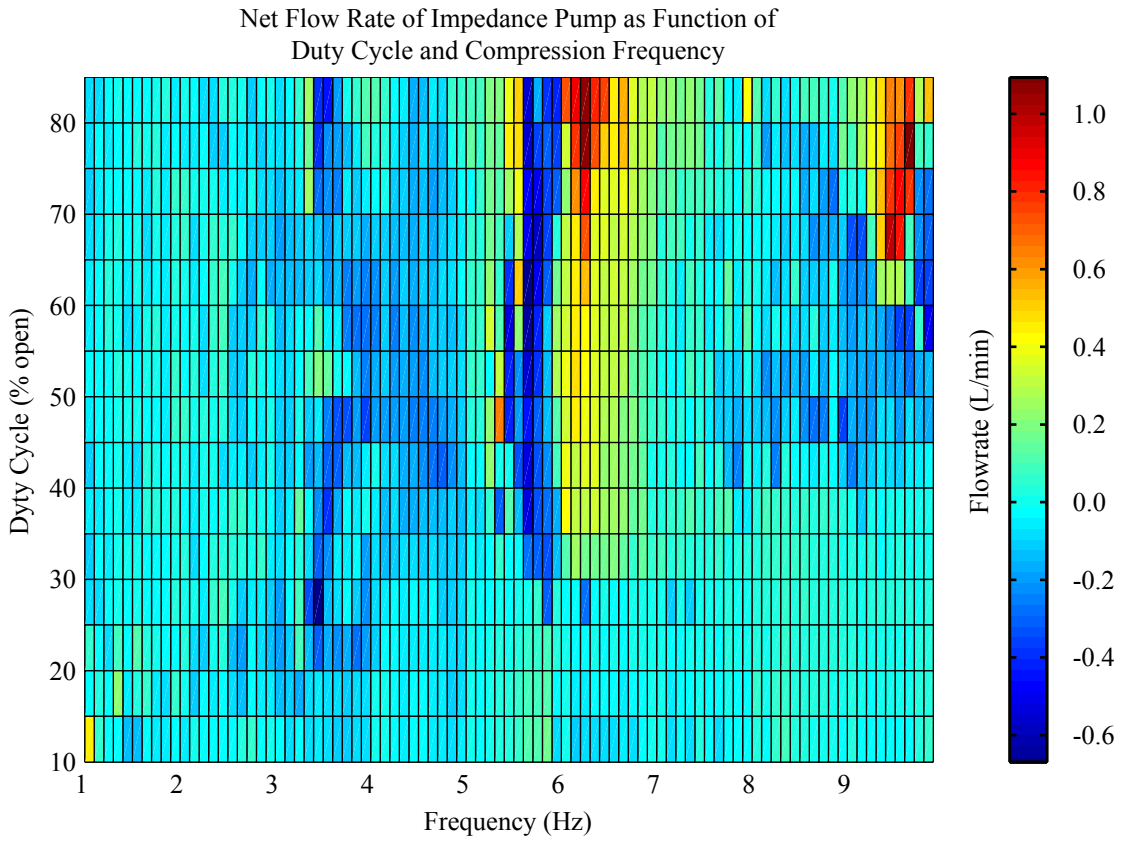

Figure 3.23: The net flow rate of the impedance pump as a function of duty cycle and compression frequency.

physically obstructed for different amounts of time and the pressure wave interaction on the tube is modified because the pressure waves can reflect off of the compression site for different amounts of time. For this configuration, the duty cycle only affects the magnitude of the net flow but not the direction or frequency response. This is caused by the obstruction to flow. In another configuration with less attenuation, the duty cycle may have more effect because the amplitude of the pressure wave will be greater when it returns to the pincher location.

3.3.7 Bulk Flow Efficiency

The efficiency of the impedance pump system may be separated into three parts: the electromechanical efficiency of the compression mechanism, the efficiency in the

conversion of mechanical to fluidic power and, finally, the pulsatile nature of the flow which requires us to determine the efficiency associated with the net flow versus pulsatile flow.

The electromechanical efficiency is dependent on the design of the compression mechanism. This loss is not a fundamental part of the pump's behavior and is therefore not addressed in this thesis. The mechanical to fluidic power can sustain a loss only in the form of heat if a restoring force is incorporated into the compression mechanism. This suggests that with proper design, this loss can be minimized relative to the pulsatile flow loss. The final loss between the pulsatile flow to net flow can be calculated in the following way:

Property	Symbol
Period of compression	T
Time	t
Pressure difference across length of pump	$\Delta P(t)$
Volumetric flow rate	$Q(t)$

Table 3.1: Variables used in calculating efficiency

$$\text{Net Power} = \frac{1}{T}\int_{t=0}^{T} \Delta P(t)dt \cdot \frac{1}{T}\int_{t=0}^{T} Q(t)dt$$
$$\text{Total Power} = \frac{1}{T}\int_{t=0}^{T} \Delta P(t) \cdot Q(t)dt$$

We consider the data set used for analyzing the transient and resonant responses of the impedance system whose bulk flow behavior is illustrated in figure 3.6. An efficiency of 15% is seen at the point of maximum net forward flow.

A typical centrifugal pump with comparable flow rates to the impedance pump tested will have an efficiency between 40% and 65% at its optimal operating point [9]. This is significantly higher than the 15% of the impedance pump. However, the advantages of a simply actuated tube over a pump requiring seals and blades may overcome this difference. In addition, for some applications, such as for mixing, a pulsatile flow is preferred over a simple flow. For those cases, the efficiency calculated

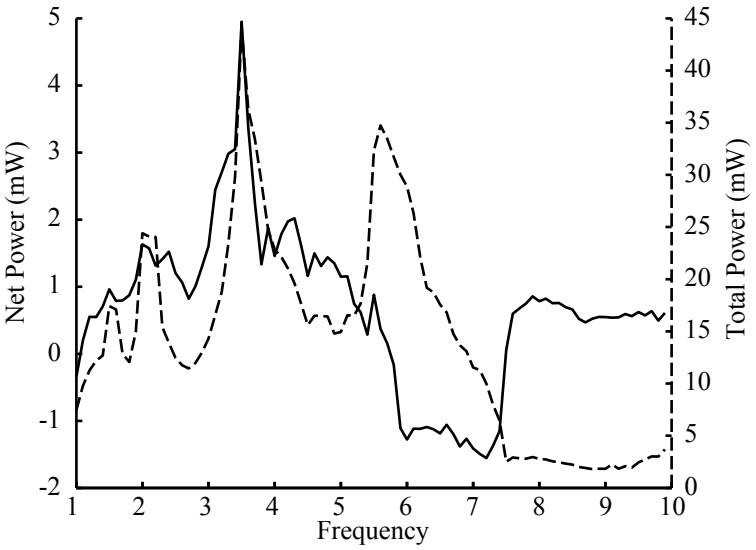

(a) The total and net fluidic power as a function of compression frequency

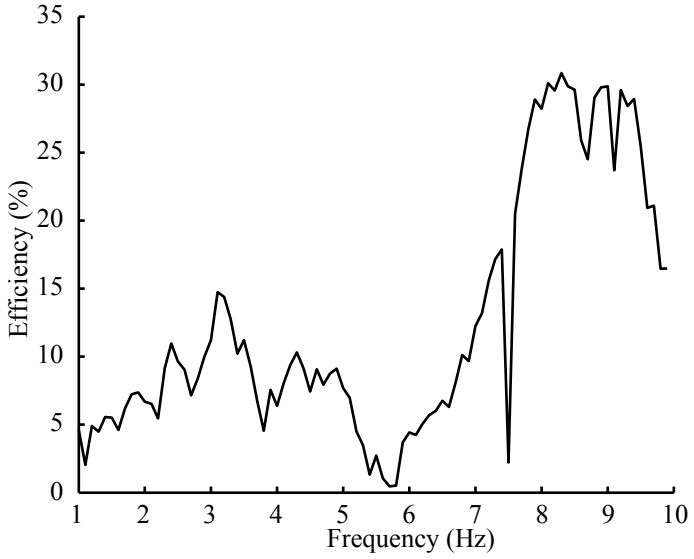

(b) The efficiency of power as a function of compression frequency

Figure 3.24: The power efficiency of the impedance pump based on the net forward and total power of the fluid as derived from the data set shown in figure 3.6

in the loss due to the pulsatile nature does not apply.

Chapter 4

Physical Model

The impedance pump functions based on wave reflections. Each time the tube is compressed, a pair of traveling pressure waves emerges from the ends of the pincher. When the waves reach a mismatch in impedance they will partially reflect. Reflections can occur at the ends of the tube or at the compression site if it is in the closed position when a reflected wave arrives. The sum interaction of these waves is responsible for the build-up of pressure across the pump. The amount of energy imparted into the fluid will depend on the size and shape of the compression as well as the amplitude of compression. The compression profile in time, both its frequency and waveform, will determine the waves generated in the system. And, the mechanical properties of the system such as the diameter, length, materials, pressure, and fluid will ultimately be responsible for the wave speed, attenuation, and the reflectance coefficient in the system.

4.1 Position of Compression

When looking at the data set in figure 3.16, a clear pattern emerges in the net flow versus frequency response of the system. The curves appear similar though at different scales. Two sets of peaks can be determined for the data set. By plotting the frequency of compression versus the position of compression of these two sets we arrive at figure 4.1(a). A similar plot can be made for the amplitude of the flow rate at those peaks. We find that the frequency of the peaks lies on a parabola, while the

amplitude lies on a cubic with symmetry about the center of the elastic section.

4.2 Dimensional Analysis

Auerbach et al. presented an analytical model for the impedance pump that requires inviscid flow and consists of a short distensible section at which active compression occurs and two rigid sections of unequal length [1]. Additionally, the solution requires the application of a constant pressure head at the boundaries of the pump. From their model arises a non-dimensional number, λ, that is predicted to be constant (table 4.2).

Property	Symbol
pressure difference across length of pump	ΔP
average flow velocity exiting pump	V
offset from center of compression	h
half the length of pump	L

Table 4.1: Variables used in calculating λ

$$\lambda = \frac{\Delta P}{0.5\rho V^2 \frac{h}{L}}$$

Upon application of this number on the data collected, we find that there is no constant line nor trend line found from this formula.

4.3 Lumped Model

Approaches taken thus far to model the behavior of an impedance pump can be divided into two broad categories: lumped models that build an analogy to known solvable systems such as electrical circuits and determine the response of those systems, and computational models that apply known fluid and structure laws to finite cells and determine the response computationally at small temporal and spatial steps. The computational results are more experimental in nature, whereas the lumped models make a prediction of the dominant mechanics.

One such lumped model is presented by Field et al. [3]. This model consists

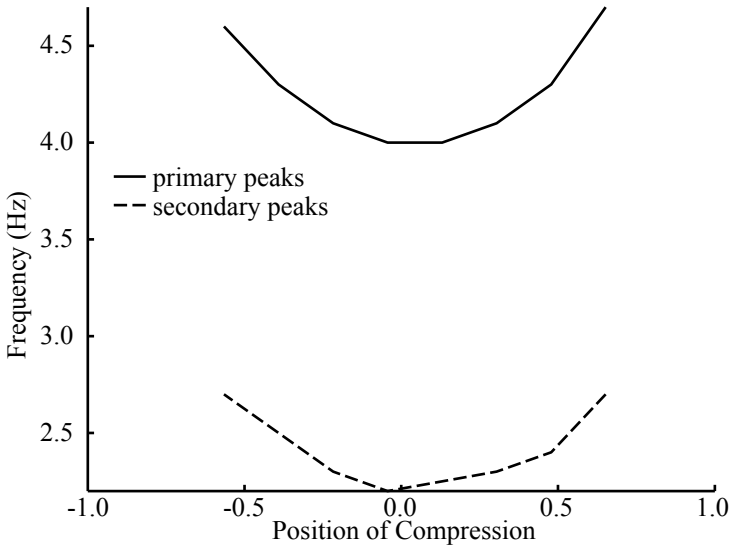

(a) Peaks in Frequency

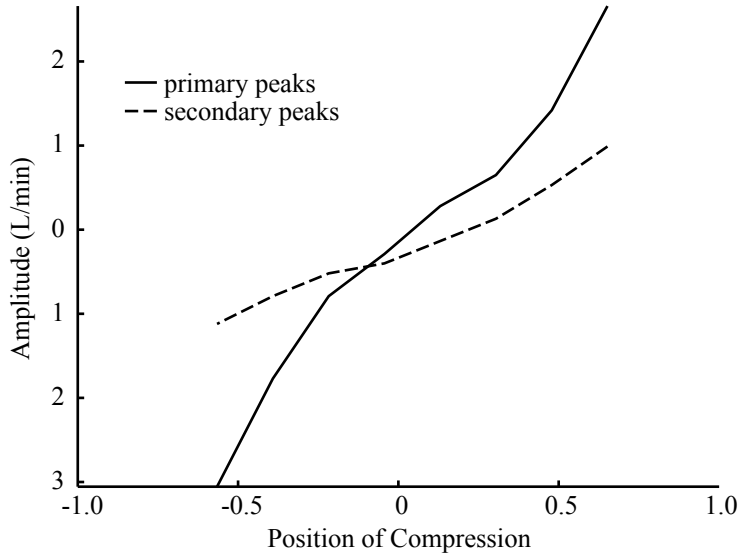

(b) Peaks in Amplitude

Figure 4.1: Effect of position of compression on the frequency and amplitude of two distinct peak sets chosen from the data set in figure 3.16. The position of the compression has been centered at and non-dimensionalized by half the length of the elastic section.

of a three-element electrical analog. A resistor represents both the viscous losses and losses due to the convergence and divergence of the cross sectional area. An inductor represents the inertia of the fluid. A capacitor represents the compliance of the surrounding vessel. All the terms are time variant, but not spatially variant. This model then uses a time variant pressure represented by a voltage to actuate the tube. This model has some interesting results: the flow and pressure have a complex periodic oscillation, the net pressure as a function of frequency displays a chaotic response, and period doubling is observed at increasing driving frequencies. However, this type of formulation cannot incorporate the wave propagation that seems to be the underlying cause for the unique frequency responses and resonant behaviors.

4.4 Wave Pulse Model

We offer a third approach to modeling the impedance pump and predicting its behavior. Experimental observation has shown us that wave propagation and reflection on the surface of the pumping element plays an important role in the behavior of the impedance pump. Starting from this point, we can create a wave model designed to mimic the wave properties of the impedance pump.

We begin with a line of fixed length that represents the length of the impedance pump along which a wave can travel.

$$-L \leq x \leq L$$

Compression parameters can be chosen including the location of the center of compression, width, period and duty cycle (table 4.2).

Property	Symbol	Range
compression location	l	$-L < l < L$
width of compression	w	$0 \leq w < L - \|l\|$
period	T	
duty cycle	d	$0 \leq d \leq 1$

Table 4.2: Compression parameters

We use the assumption that a pair of pressure waves are emitted each time the "tube" is compressed. These waves are allowed to travel along the line reflecting any time they reach the ends of the line or the compression location if in the closed position. Additional configurable parameters of the model include the time step between calculations, wave speed, total simulation time, amplitude decay constant, reflectance coefficient, initial wave amplitude, pulse width, and pulse waveform (table 4.3).

Property	Symbol	
time step	dt	
wave speed	c	
total simulation time	sim_t	
amplitude decay constant	r	$0 \leq r \leq \frac{1}{dt}$
reflectance coefficient	R	$0 \leq R \leq 1$
initial wave amplitude	A_0	
pulse width	p	
waveform	$P(x)$	$P(x) = e^{-\frac{2x}{p}^2}$

Table 4.3: Additional model parameters

For each wave pair emitted, their start time, travel time, total distance traveled, directions, amplitudes, and positions are computed for small temporal steps.

- The **start time** for each pair is dependent on the compression period and is an integer multiple of the period.

$$iT$$

- The **travel time** is incremented by dt for each time step above the start time. It is equivalent to

$$= \begin{cases} t - iT & \text{for } t \geq iT; \\ 0 & \text{for } t < iT; \end{cases}$$

- The **total distance traveled** is the wave speed multiplied by the travel time.

$$= \begin{cases} c(t - iT) & \text{for } t \geq iT; \\ 0 & \text{for } t < iT; \end{cases}$$

- The **direction** of each wave changes sign for each reflection encountered.

$$\text{dir} = \begin{cases} -1 & \text{for a wave moving in the negative x-direction} \\ 1 & \text{for a wave moving in the positive x-direction} \end{cases}$$

- The **amplitude** of each wave is based on an initial amplitude, chosen decay constant, and reflectance coefficient. Each wave is subjected to exponential decay in the form

$$A(t) = A(t - dt)(1 - r dt)$$

And, for every reflection at the ends, the amplitude is decreased according to the reflectance coefficient such that

$$A(t) = R \cdot A(t - dt)$$

- Finally, the **positions** are determined based on a fixed wave speed which in a real pump would be a result of the material properties, fluid properties, and transmural pressure. The position is therefore

$$\text{pos}(t) = \text{pos}(t - dt) + \text{dir } cdt$$

In the event of a reflection at a site x, the position is adjusted according to

$$\text{pos}(t) = -(\text{pos}(t - dt) + \text{dir } cdt) + 2x$$

A Gaussian waveform is applied about the calculated positions of all the waves and is reflected in the same manner as the wave position if it crosses a reflection site.

$$P(x) = e^{-\frac{2x}{p}^2}$$

All of the waves are then summed along the length of the line divided discretely into steps of length dL to form a spatial wave profile for each time step. The difference in

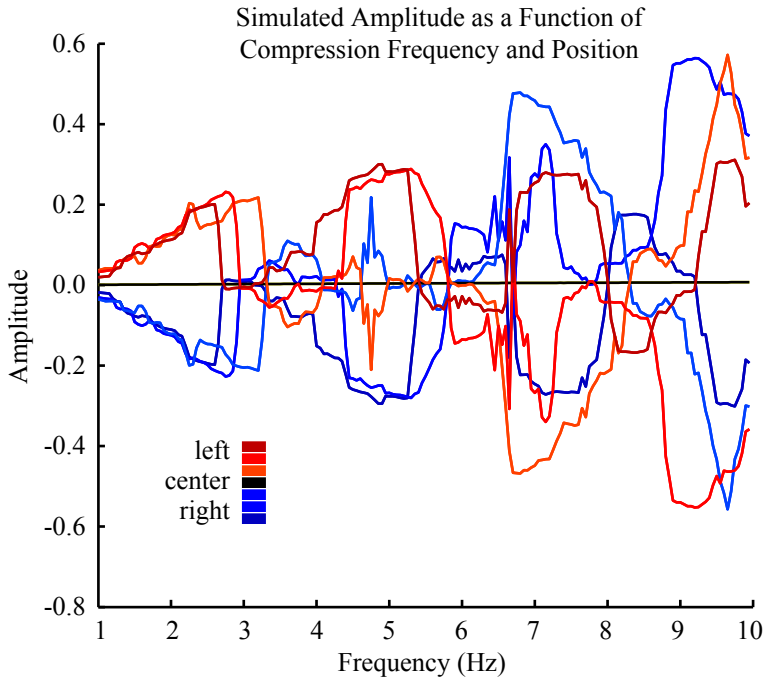

Figure 4.2: Simulation of wave amplitude difference as a function of compression frequency and position.

the summed wave amplitude at the ends of the line represent a value proportional to the pressure head of a similar pump. Once an equilibrium is reach a mean value of the amplitude difference can be taken for varying compression frequencies.

The model was implemented using C++ code. We find similar results to those of the experiments: the frequency response in the time-averaged amplitude difference across the length of the model shifts with the position of compression and is symmetric about the center (figure 4.2); and the frequency response increases linearly with the wave speed (figure 4.3). Additional results from the simulation show that the pulse width greatly affects the amplitude of the difference across the length of the pump (figure 4.4). The reflectance coefficient induces a similar behavior. As the reflectance coefficient increases, so does the amplitude difference across the length. As the reflectance coefficient goes to zero, no net difference is found across the pump (figure 4.5).

A comparison can be made between the experimental results and the simulation

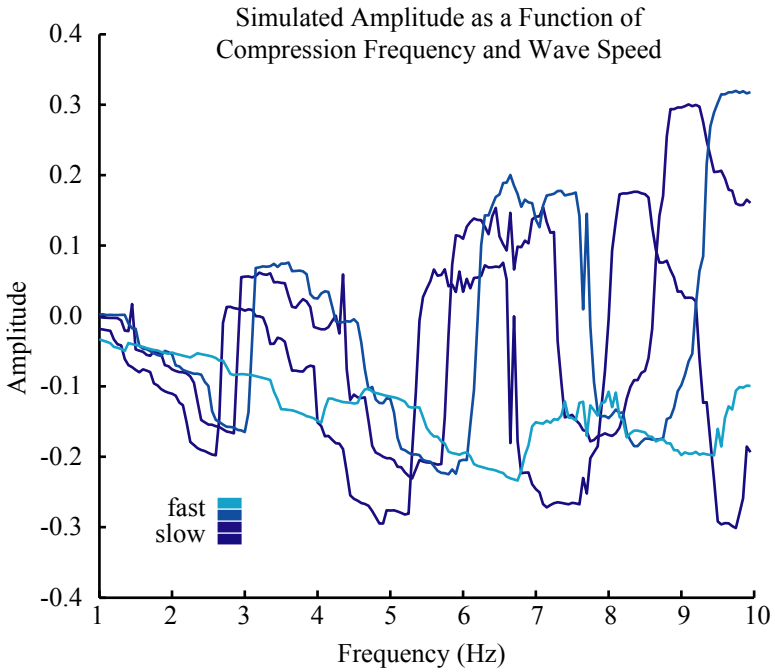

Figure 4.3: Simulation of wave amplitude difference as a function of compression frequency and wave speed.

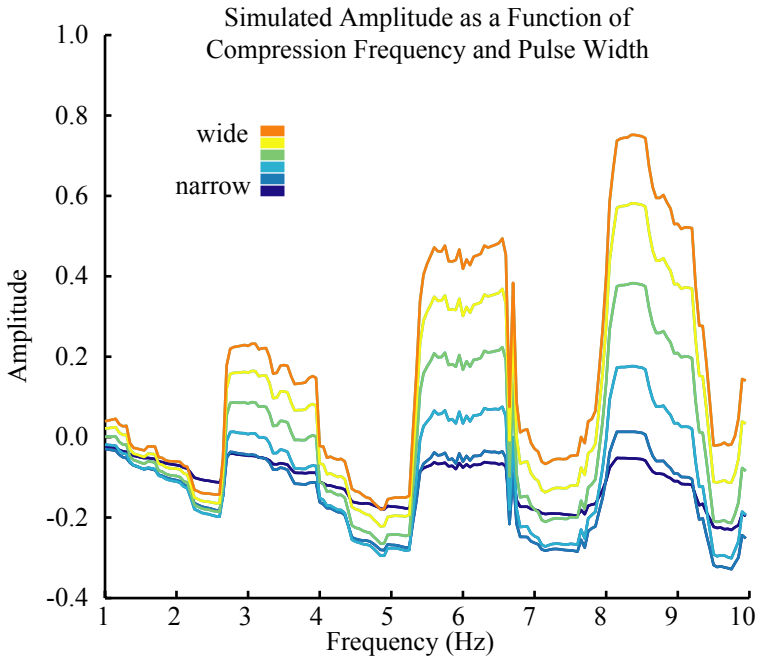

Figure 4.4: Simulation of wave amplitude difference as a function of compression frequency and pulse width.

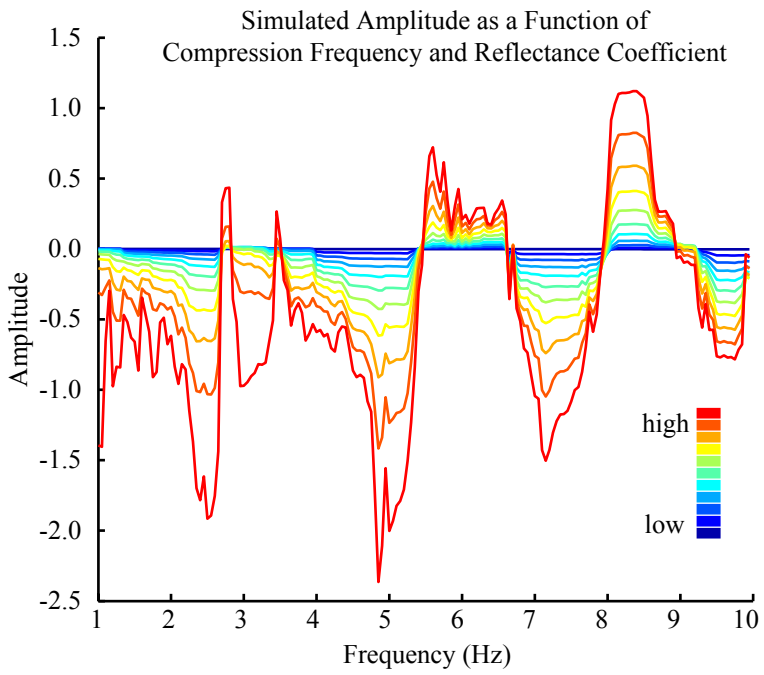

Figure 4.5: Simulation of wave amplitude difference as a function of compression frequency and reflectance coefficient.

using parameters in the range known to be accurate for a specific experiment (table 4.4). Many of the parameters are easily applied from the experiments. To maintain convention used in the experiments, duty cycle is the fraction of the compression period that the pinchers are not in contact with the tube. As was discussed in section 3.2.1, the pinchers only remain in contact with the tube during the compression and not retraction when the motorized compression mechanism is used and the duty cycle had been adjusted accordingly. The parameters that remain unknown are the amplitude of the pressure wave, the waveform including its shape and width, the amplitude decay constant, and the reflectance coefficient. If we do not concern ourselves with the scale of the simulated results, but instead we worry just about the shape, we can safely select the initial wave amplitude, pulse width, and reflectance coefficient without affecting the overall shape. This leaves the shape of the waveform and the amplitude decay constant up to interpretation. The shape chosen was a simple Gaussian loosely based on the ultrasound images of the tube wall. The decay constant was

also loosely based the ultrasound images, then further refined to fit the experimental results with the simulated results as closely as possible.

Parameter	Experiment	Simulation
Total time	10 sec	10 sec
Time step, dt	NA	10 msec
Wave speed, c	60 $\pm$ 10 m/sec	50 m/sec
Length of tube, $2L$	15 cm	15 cm
Length step, dL	NA	0.01 cm
Compression location, l	-5.1 cm	-5.1 cm
Width of compression, w	2.5 cm	2.5 cm
Duty cycle, d	70%	70%
Initial wave amplitude, A_0	unknown	3
Waveform, $P(x)$	unknown	3 cm wide Gaussian
Amplitude decay constant, r	unknown	0.2
Reflectance coefficient, R	unknown	0.5

Table 4.4: Parameters used for comparing experimental and simulated results.

The simulated results maintain most of the characteristics found in the experiments. There are distinct, sharp peaks at select compression frequencies. Those peaks lie at approximately the same locations. However, it appears that a linear term, if added to the simulated results, would create a more accurate model of the experiment. Capturing this effect will require further modeling. The model can be extended by incorporating dispersion in the form of a time variant waveform. Additional work is necessary to incorporate the interaction with the fluid. For this part, we can borrow from the lumped model techniques and add resistance and impedance. Furthermore, in the real experiments, there is a maximum input that can be exerted on the tube. If the tube is already collapsed at the location of the compression, no work is done if it is compressed again at that time. The disparity between the simulated and experimental results caused by this effect grow with the frequency of compression.

What remains unique and quite exciting about this model is that it begins with wave propagation as its mechanism. It shows that standard wave propagation and wave reflection can be the mechanisms that build a net pressure across the length of the pump. The force causing the wave propagation and the mechanism forcing the reflections are secondary.

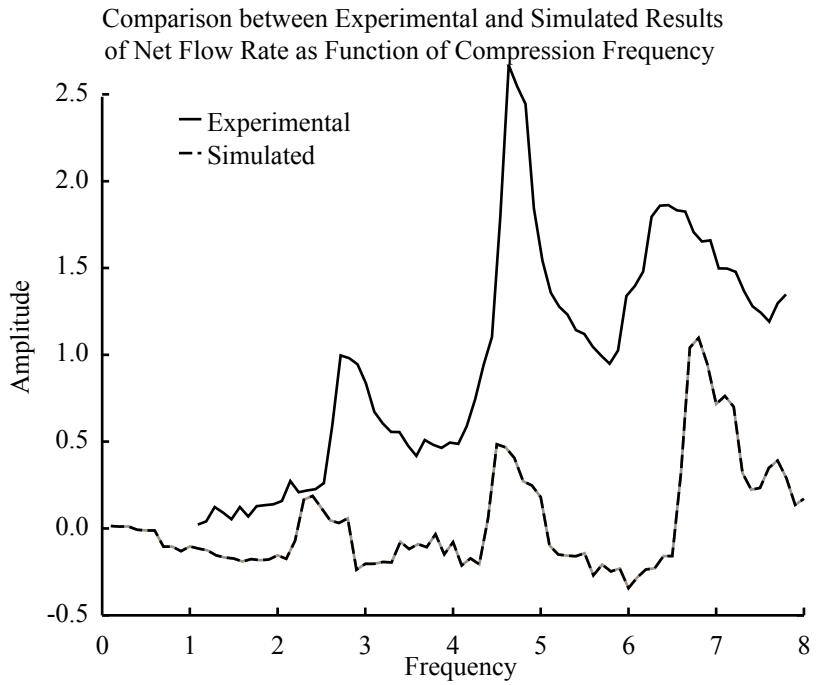

Figure 4.6: Simulation of wave amplitude difference as a function of compression frequency compared with experimental results.

Chapter 5

Concluding Remarks

In the excitement of the impedance pump phenomenon, a number of publications have been written trying to model the behavior of a valveless tube pump. Nevertheless, little had been done experimentally to determine the nature of the pumping being modeled. Presented in this thesis are the experimental results that provide the basis for comparison between models and insight into the dominant parameters that are critical in its function. Though this phenomenon has been known for many years and has inspired interest in modeling its behavior using analytical and computational means, no one has actually looked at it in-depth experimentally. Previous investigators were unable to validate their results, capture unique behaviors, and focus on the parameter space that is integrally bound with the impedance pump. Computational studies are time-consuming and rely on the careful application of boundary conditions to achieve a meaningful result. Analytical work is also complex, and relies on the simplification of a phenomenon to make the problem tractable. The experimental results we have collected provide a new perspective on the problem of the impedance pump and can now serve as a foundation for future modeling work.

Behaviors intrinsic to the functioning of the impedance pump have been demonstrated. Imaging of the wall motion shows wave propagation and reflection at the tubing interfaces. The compression is seen to be in phase with the wall motion during peak net flow. This alludes to the resonant behavior observed in the response to an impulse of the system, from the net flow rate as a function of compression frequency, and from the FFT's of the flow rate at varying compression frequencies. Transient

response measurements show that it may take up to 5 seconds to build to a steady net flow. This is critical for use in computational modeling that will require where computing power still limited. Pressure flow relationships at the exit of the impedance pump demonstrate lower energy input required during resonance than when off resonance. A double periodic response at high frequencies is also seen. The feature most over-emphasized in previous models is the use of elasticity as a form of restoring force. We have shown elasticity is not specifically required and that any restoring force will suffice for a pumping effect to occur.

Bulk flow responses under a variety of conditions have been measured. The effects of the frequency of compression, position of compression, and transmural pressure each demonstrate the importance of wave propagation in the fundamental functioning of impedance pumps. Variation in the width of compression changes the rate of volume displacement by the pinchers, but does not affect the wave speed so the peaks in the frequency response of the net flow rate remain steady while the amplitudes differ. Adjustment of the systemic resistance and duty cycle shows that the pumping phenomenon observed is a true pump capable of sustaining a net pressure head and compensating for flow resistance rather than a mathematical curiosity.

An appropriate model describing the function of the impedance pump can provide the means to better identify an impedance pump system. There are a number of distinguishing features of impedance driven flows, which can be used in this identification. An impedance pump requires an active element only at one position (not in the center) along the length of the wave-propagating section. The wave speed traveling on the tube does not necessarily have the same velocity, nor must it be in phase with the flow rate. The flow exiting an impedance pump is pulsatile. And, the net flow rate has a non-linear relationship to the frequency of activation with characteristic peaks and flow reversals dependent on the natural resonant frequency of the system.

A model can also be used in the design of pumping systems. Such work is already under way with applications ranging from cardiac assist devices to micro-fluidic pumps to the better understanding of naturally occurring systems such as the zebrafish embryonic heart.

Appendix A

Constants and Conversions

Units presented in this dissertation were the native units of measurement by the manufacturers and instrumentation. Therefore, a chart of conversions has been provided for the reader.

Property	Symbol	Value
Density	ρ	10^3 kg/m^3
Dynamic (absolute) viscosity	μ	10^{-3} kg/(m s)
Speed of Sound	c	1500 m/s

Table A.1: Properties of water

Property		
Pressure	1 mm Hg	1 torr
Pressure	1 mm Hg	133.28 Pa
Pressure	1 mm Hg	1.934x10^{-2} PSI
Pressure	1 mm Hg	0.5353 in H_2O
Volume	1 L	10^3 cm^3 (cc)
Volume	1 L	10^{-3} m^3
Volume	1 L	61.02 in^3
Volume	1 in^3	16.39 cm^3 (cc)
Flow rate	1 L/min	1.67x10^{-5} m^3/sec
Flow rate	1 L/min	16.67 cm^3/sec
Flow rate	1 L/min	1.017 in^3/sec
Length	1 inch	2.54 cm

Table A.2: Unit conversions

Glycerol Sol. (% by Mass)	Kinematic Viscosity (cP)
0	1.004
0.5	1.012
1	1.022
2	1.045
3	1.068
4	1.092
5	1.116
6	1.143
7	1.171
8	1.201
9	1.232
10	1.263
12	1.330
14	1.401
16	1.480
18	1.566
20	1.661
24	1.882
28	2.136
32	2.449
36	2.839
40	3.326
44	4.005
48	4.833
52	5.895
56	7.311
60	9.264
64	11.73
68	15.70
72	23.28
76	33.88
80	49.57
84	69.18
88	119.9
92	310
96	624
98	939

Table A.3: Kinematic viscosities of glycerol solution in H_2O concentrations

Appendix B

Rotary Viscous Pump

B.1 Introduction

The limitations of the current technology in left ventricle assist devices (LVADs) led us to explore new design concepts leading to the viscous pump. The most significant improvements in this design are the prospect of not causing hemolysis, scalability, and of its capability of being flexible and thereby more compliant with the human body.

The basic mechanism of the pump consists of two primary parts: the first is a tube, open at both ends, with helical grooves on the inner surface, the second is a smooth shaft inside the tube that is spun by a motor. As the shaft rotates, it drags the fluid with it and the helical grooves guide the flow in a specified direction.

What differentiates this design from an Archimedes pump or a traditional pump is that there are no sharp surfaces moving in the fluid. We anticipate that this will minimize hemolysis. Other benefits of the design include the ability to make it flexible, in turn making it easier to implant and more compliant as an internal device.

B.2 Methods

The prototype of the pump was first made using stereolithography, a technique that creates polymer models from a computer design. Because of the limitations in the resolution of stereolithography, the design used in these experiments used a 1/2-inch

Figure B.1: Photograph of a stereolithography model of the rotary viscous pump.

shaft that was connected to an external brushless motor. The pump was incorporated into a test loop consisting of two pressure transducers located at the inlet and outlet of the pump, a transonic flow transducer, a reservoir of fluid, and an adjustable ball valve. Sections of the loop were made from Tygon 3603 tubing and connected with quick release connectors.

Two sets of data were collected for each case explored. In the first test, the ball valve was left completely open while the angular velocity of the shaft was adjusted by steps of approximately 1000 rpm. Ten samples were taken for each data point over ten seconds. Measurements were taken through a National Instruments DAQ board and recorded using LabVIEW. Data collected included the inlet pressure, outlet pressure, flow rate, and the power consumption of the motor.

In the second test, the angular speed of the shaft was set to the constant rate of 7650 rpm. In this case, however, the opening of the ball valve was adjusted in steps of 15 deg to modify the resistance of the loop. The data were collected in the same manner as the first test.

B.3 Stereolithography Results

A variety of design parameters were modified and tested. To begin, we tested the performance of our initial design with both water and 31% by volume glycerol solution corresponding to a viscosity of 3.082 g/cm-sec, similar to that of blood (figure B.2).

The pump performed better with the glycerol solution by increasing the flow rate for a given angular velocity by approximately 10%. The pressure head at a given flow rate was about 40% greater for the glycerol solution than the water.

For the experiments that followed, the pump with the best results from the previous experiment was chosen and modified. This was because the number of pumps that would have to be produced in order to collect all permutations of the design would have been too large. As a result, all the further experiments were completed with 31% glycerol solution.

The other parameters tested include the number of grooves within the pump (figure B.3), the pitch of the grooves (figure B.4), the depth of the grooves (figure B.5), the length of the pump (figure B.6), and the roughness of the surfaces both on the shaft and in the helices (figure B.7). The gap distance between the shaft and helices was maintained as constant as the accuracy of stereolithography would allow. All the parameters had dramatic effects on the performance of the pump. The grooves, to our surprise, appeared to improve the performance of the pump the shallower they were, despite the decrease in the inflow area. However, the deviation in gap distance may play a critical role in this result. Increasing the number of grooves, as well as increasing the length, improved the performance of the pump with less than linear success. The optimal pitch found was 58 deg from the axis testing at increments of 8 degrees.

B.4 Dimensional Analysis and Similitude

Dimensional analysis was performed to predict the pump's performance at smaller scales. The best performing stereolithography data set was chosen for the analysis. The effective angular velocity (Ω), flow rate (Q), and pressure head (P) were determined by holding the Reynolds number [1] constant. The density and viscosity would be fixed for all size scales. The characteristic velocity and the characteristic length

[1] The Reynolds number is defined as $\mathrm{Re} = \frac{\rho V L}{\mu}$ where ρ = density, V = characteristic velocity, L = characteristic length, and μ = dynamic (absolute) viscosity.

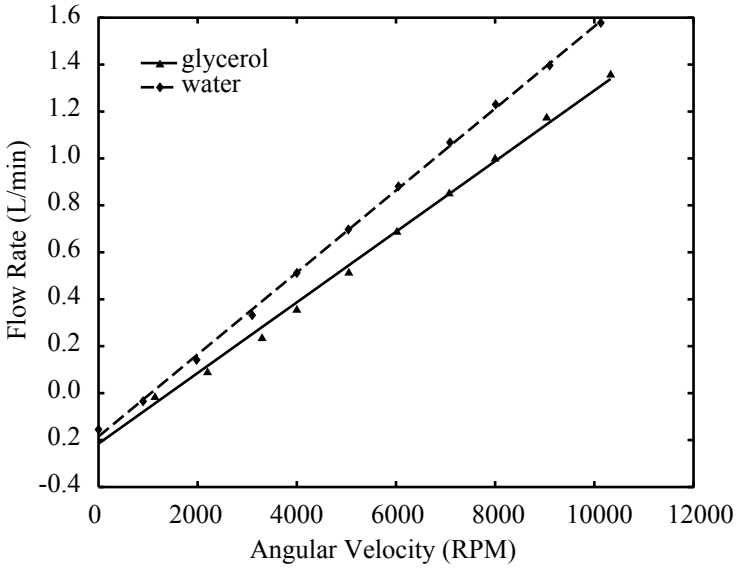

(a) Constant Resistance

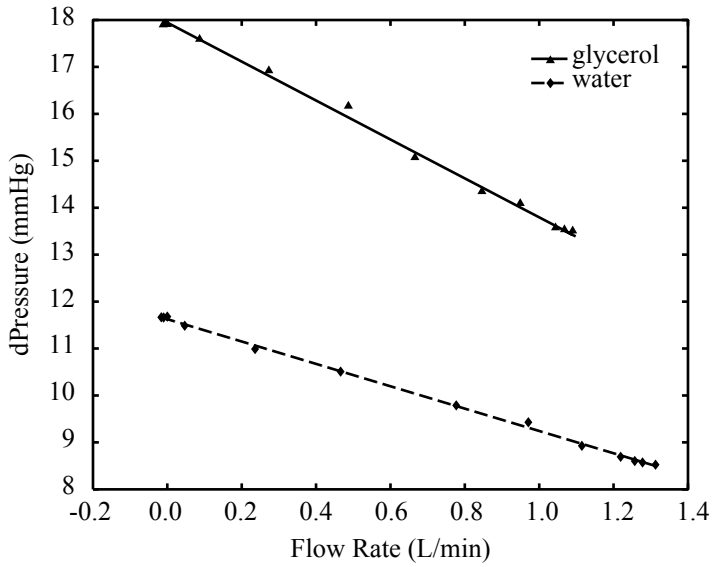

(b) Constant Angular Velocity

Figure B.2: Performance of rotary viscous pump as a function of viscosity.

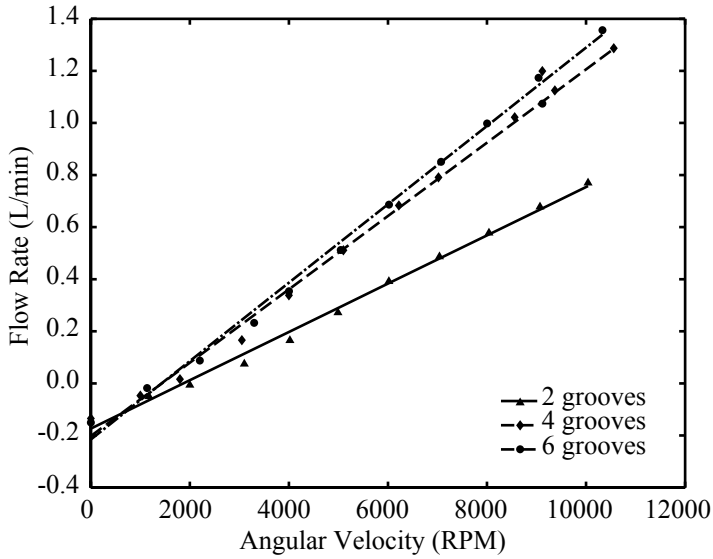

(a) Constant Resistance

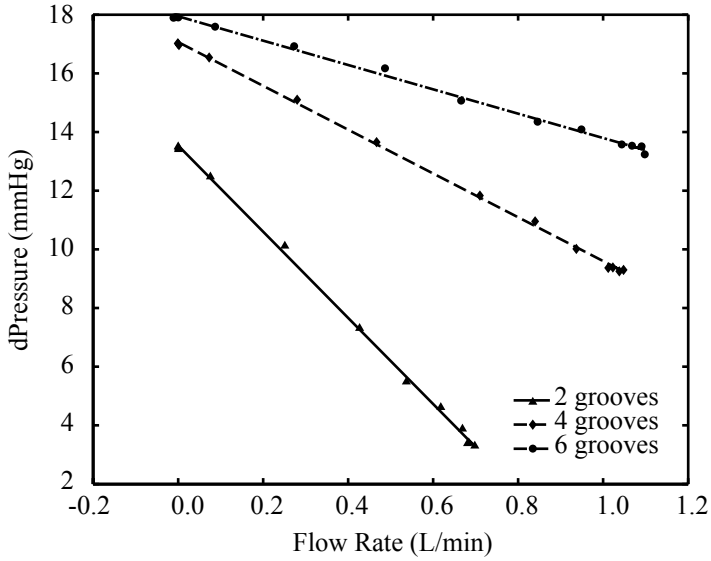

(b) Constant Angular Velocity

Figure B.3: Performance of rotary viscous pump as a function of number of grooves.

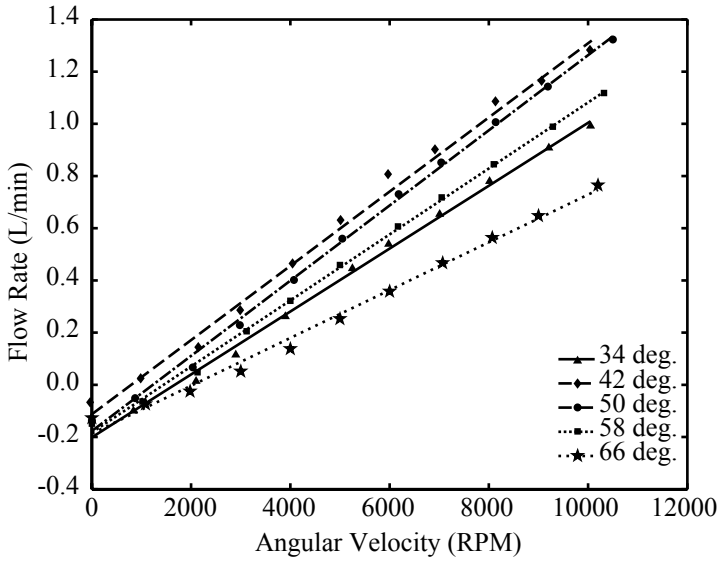

(a) Constant Resistance

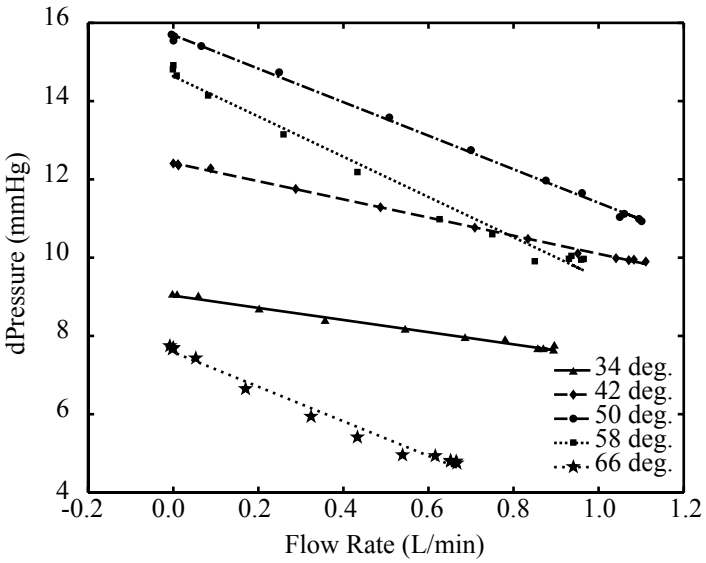

(b) Constant Angular Velocity

Figure B.4: Performance of rotary viscous pump as a function of groove angle.

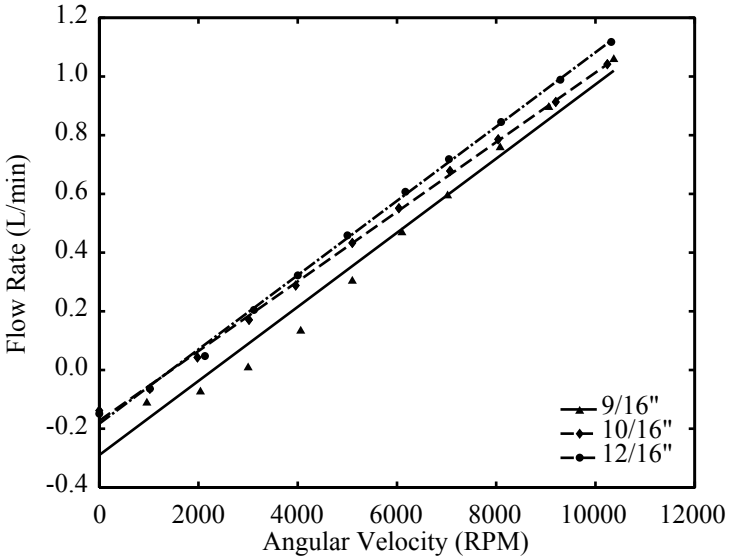

(a) Constant Resistance

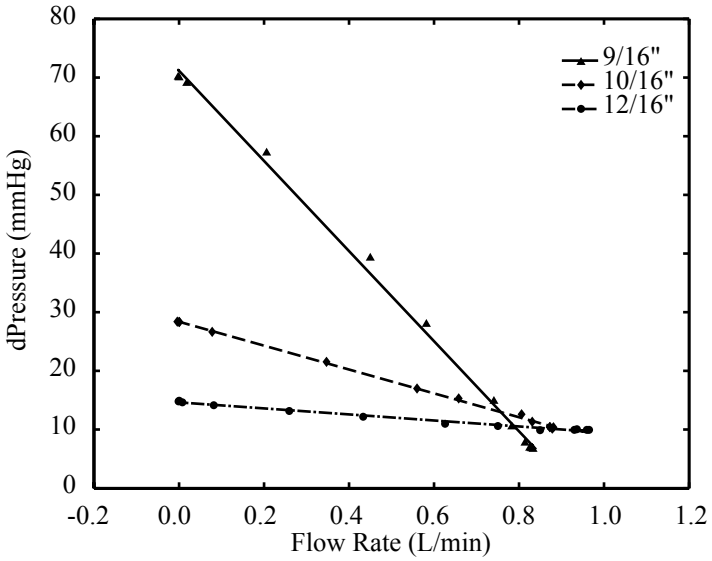

(b) Constant Angular Velocity

Figure B.5: Performance of rotary viscous pump as a function of depth of grooves.

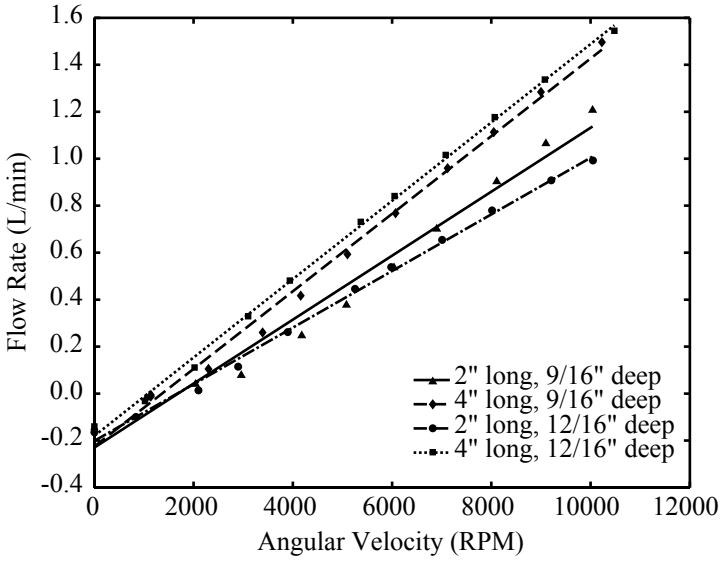

(a) Constant Resistance

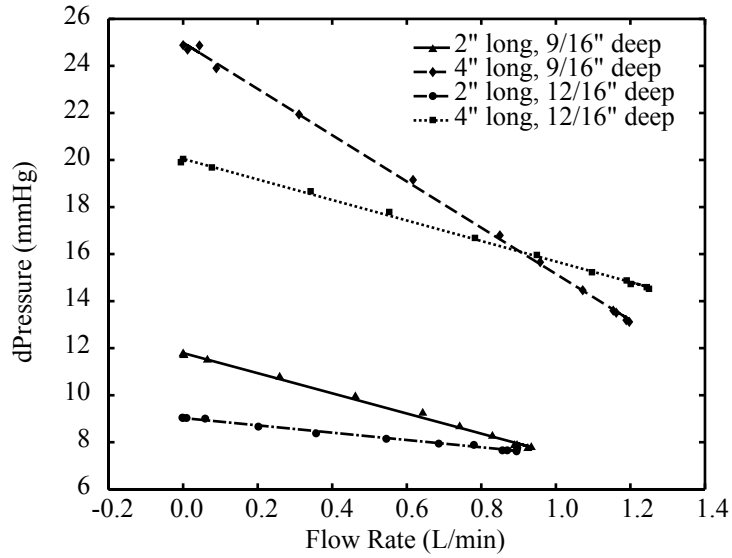

(b) Constant Angular Velocity

Figure B.6: Performance of rotary viscous pump as a function of length of pump.

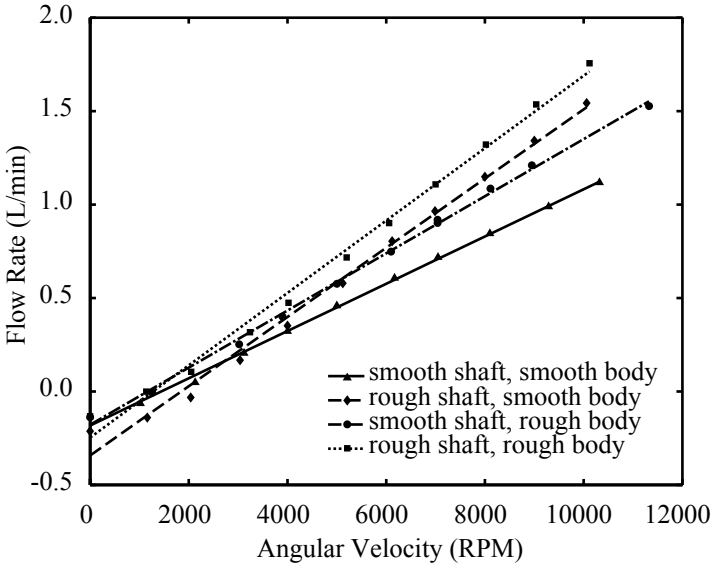

(a) Constant Resistance

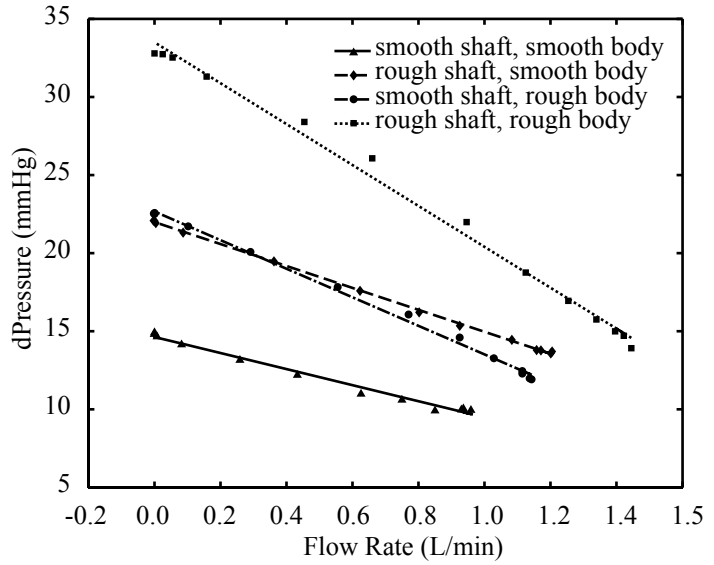

(b) Constant Angular Velocity

Figure B.7: Performance of rotary viscous pump as a function of surface roughness.

chosen were the surface speed and the radius of the internal shaft, respectively. If we define α as the characteristic length of the predicted pump a to that of the known pump b ($\alpha = \frac{L_a}{L_b}$) we find that the effective angular velocity is

$$\Omega_a = \frac{\Omega_b}{\alpha^2}$$

Assuming that the flow rate will be identically proportional to L^2V the effective flow rate becomes

$$Q_a = \alpha Q_b$$

The pressure is determined by

$$P_a = \frac{P_b}{\alpha^2}$$

B.5 Other Manufacturing Techniques

Given the encouraging results of the first round of testing we decided to pursue the scaling of the design to a biologically relevant size that could be implanted through the femoral artery. Because stereolithography does not provide sufficient accuracy, other manufacturing techniques had to be considered. Among those were thermal plastics extrusion, latex dipping, and silicone molding. Thermal plastics extrusion proved to be too expensive to try. Latex dipping was only partially successful. The part could be made, but the latex material was sticky and inaccurate. Also, it took two days to complete one part. Eventually, we used a two-part silicone molding technique that could reliably produce a part in 24 hours.

B.6 Silicone Designs

The first step to the silicone molding process is to design the mold. Our mold was machined from aluminum so that it would be accurate and reusable. The longest length that the interior mold could be made while maintaining a maximum diameter of 1/4 inch was 4 inches. The silicone used was a two part formula, General Electric's

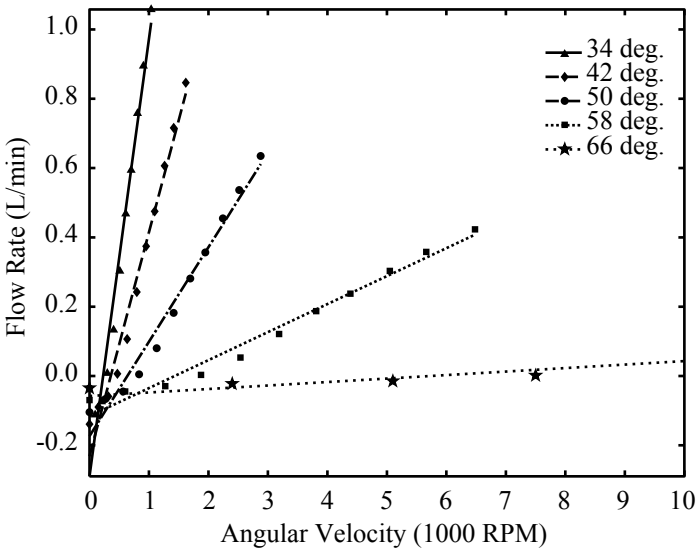

(a) Constant Resistance

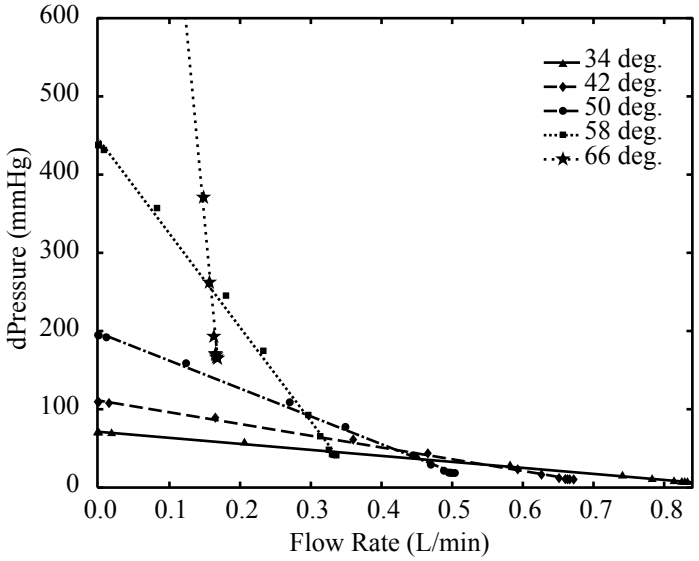

(b) Constant Angular Velocity

Figure B.8: Similitude results based on perfomance of rotary viscous pump.

RTV615. This particular silicone had the necessary combination of characteristics. It was rigid, easily poured before setting, and bio-compatible. In order to create a smooth and consistent texture to the mold, the silicone mixture, before setting, needed to be vacuum-pumped to remove the air bubbles. In addition, a large surface area exposed to the air and a shallow mold help the irregularities settle out during the setting period.

The experiments performed with the new silicone design are analogous to those done on the stereolithography prototypes. First the pump was tested at various rotational speeds up to 10,000 rpm with minimal loop resistance. The inlet and outlet pressures were measured, as well as the flow rate. A second test was performed where the rotational speed of the shaft was held constant and the loop was shut by pinching the Tygon tube closed.

B.7 Silicone Results

The experiments performed on the silicone rubber design showed that scaling of the pump is possible. The geometry for the mold was chosen such that the resulting pump matched as closely as possible to the best performing stereolithography pump. This corresponded to a pitch of 58 degrees and a groove depth of 1/32 inches.

The silicone pump had a flow rate that was linearly proportional to the rotational velocity. The flow rate corresponding to a constant surface velocity of the shaft for the silicone pump was comparable to that of the analogous stereolithography pump. The resistance of the loop was minimal, creating an immeasurable pressure gradient across the pump. However, when the loop was closed, the pressure increased up to 20 mm Hg.

B.8 Acknowledgements

I would like to thank the IRC Grubstake program for supporting this research. Also, Bahram Valiferdowsi for his work prior to my participation in the design and his

continued collaboration following. In addition, I would like to acknowledge Barbara Hirtz and Ng Kuang (Nathaniel) Chern for their continued work on the rotary viscous pump. Barbara worked with the silicone molded design. Nathaniel used a machined Delrin pump. Both their efforts focused on the hemolysis testing for blood use.

Appendix C

Flow Visualization

C.1 Digital Particle Image Velocimetry

Digital particle image velocimetry (DPIV) is a flow imaging technique that can provide quantitative data about a flow field in two dimensions. The fluid of interest is seeded with small particles that can fluoresce in laser light. A sheet of laser light is shown through the plane of interest and photographed at a known frame rate. The images are then divided into small regions. By computing a cross-correlation between these regions in consecutive frames, the net velocity of that region can be calculated. A number of methods can be used to improve upon the resolution of this technique. However, it remains limited to flows in which the fluid is optically clear and accessible.

C.2 Ultrasound Doppler

Traditional ultrasound images are captured by measuring the time for a longitudinal ultrasound wave to reflect from a density interface. Flow velocities can then be determined by measuring the Doppler shift of the reflected signal [21]. This technique can be used to measure flows only in the radial direction from the ultrasound probe (figure C.1(a)).

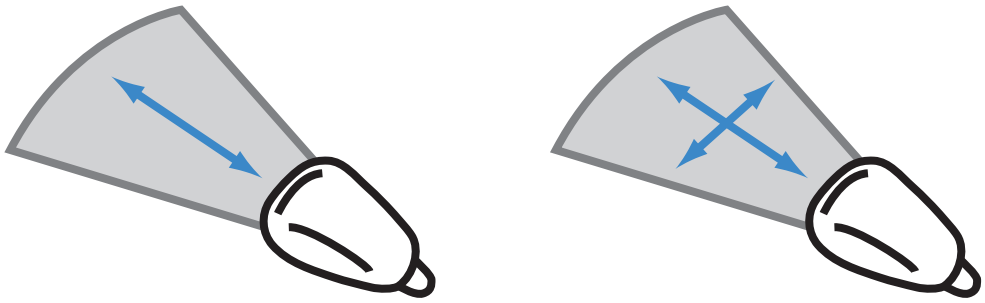

(a) ultrasound Doppler

(b) digital ultrasound speckle image velocimetry

Figure C.1: Ultrasound Doppler and DUSIV velocity directions

C.3 Digital Speckle Image Velocimetry

Digital ultrasound speckle image velocimetry (DUSIV), a hybrid between ultrasound imaging and digital particle image velocimetry, is a technique for obtaining two-dimensional flow field data. The ultrasound can be used to take images of a flow through an optically opaque body. By seeding the flow with particles that reflect ultrasound waves, one can obtain images similar to those used for DPIV (figure C.1(b)).

There remain a number of critical differences in ultrasound images that distinguish them from DPIV:

- The images acquired by ultrasound are captured in polar coordinates. This results in non-uniform resolution of the image when transformed into Cartesian coordinates.

- The individual particles are not resolved in the ultrasound images. Instead, regions in the flow where the density of particles is higher collectively reflect the ultrasound and are realized as speckles in the image.

- The pixels of the image are captured sequentially. This means that the time at which one pixel of the image was taken is not the same as the time another pixel was taken. However, the time step between any pixel in one frame and the same pixel in another frame should be constant for all pixels.

Though the implementation of DPIV and DUSIV may vary from software package to package, the math is essentially the same. Two images are acquired at a time difference of τ. The image is broken down into smaller interrogation regions. The corresponding interrogation regions between the two images are compared by computing the two-dimensional cross correlation of the intensity. This is equivalent to computing the convolution of the two images in frequency space:

$$\Phi_{fg}(x,y) = \int_{-\infty}^{\infty}\int_{-\infty}^{\infty} F(\xi+x,\zeta+y)G(\xi,\zeta)d\xi d\zeta$$

Here, $\Phi_{fg}(x,y)$ represents the cross-correlation function of the intensities of the regions f and g whose Fourier transforms are F and G. In reality, the images are finite in size (a,b), so the cross correlation need only be computed for the width and height of the region. The maximum of the cross-correlation function is then determined.

By knowing the time τ between the images captured and the maximum correlation of the two regions, a local velocity can be inferred. This is performed for regions covering the entire image and results in a velocity vector field.

DUSIV can be used to image flow through any material that transmits ultrasound. However, the probe must be in sonic contact with the body that it is imaging. This can be accomplished by using a transmitting gel, or by submerging the object of interest and the probe underwater.

Appendix D

Edge Detection Documentation

I have written, with the support of Dave Benson, a program to detect the walls of the elastic tube as imaged by the ultrasound machine. The software relies of a set of assumptions about the image to simplify the task:

- There will be two distinct walls, approximately horizontal in the images.
- The walls appear brighter than the background.
- The only other artifacts in the image are noise and speckles.

D.1 Algorithm Overview

- The original, grayscale, polar coordinate image is read from a file into an array containing the pixel data (figure D.1(a)).
- The image is box-blurred in the vertical direction to reduce noise (figure D.1(b)).
- The blurred image is searched for local maxima. These points have intensity values higher than the points directly above and below and have an overall intensity at least half the maximum intensity in the image (figure D.1(c)).
- These local maxima are linked into chains by their nearest neighbor within a search area (figure D.1(d)).
- The number of chains above a minimum length is counted.

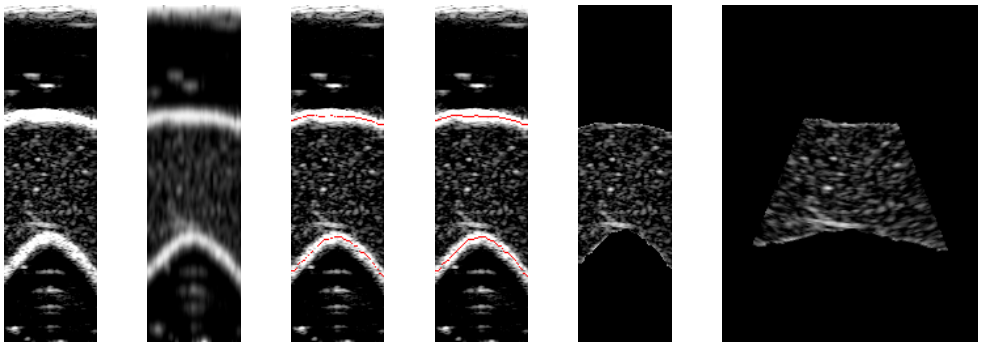

(a) (b) (c) (d) (e) (f)

Figure D.1: Processing steps of the edge-detection software (left to right: original image, box-blurred, maxima points located, maxima points linked into a chain, original image masked, coordinates converted from polar to Cartesian)

- The process is repeated by successively blurring the image until there are only two chains that match the minimum length criteria. Those chains represent the edges of the tube.
- The original image is then masked on the walls and outside the tube based on the edge locations found (figure D.1(e)).
- The masked image is transformed from polar coordinates to Cartesian coordinates for use with the DUSIV software (figure D.1(f)).

D.2 Using the Program

To compile the program, one must have a C compiler, glib 1.2, and a few other C libraries. Use the command:

```
prompt: gcc -o edgefind edgefind.c ‘glib-config --cflags --libs‘ -lm
```

Once compiled the program can be run in a shell by typing:

```
prompt: edgefind < input.pgm > output.ppm
```

The program will use the file, `input.pgm` as its input and `output.ppm` as the output file. In order to perform this task on many bitmap files, one can use the

shell script `do-all` on any computer running a bourne shell. This script requires imagemagick to convert BMP to PGM files. It then executes the ultrasound program on all the PGM files and creates PPM output files with the same name. Finally, it executes the program `ppm2raw` to convert the ppm files to raw files with the width and height information appended to the file name. This prepares the file for use with the DPIV software.

D.3 Global Constants and Variables

`CHAIN_SEARCH_WIDTH` is the width to the right or left of a pixel in which to search for another chain pixel.

`CHAIN_SEARCH_HEIGHT` is the the height to the top or bottom of a pixel in which to search for another chain pixel.

`CHAIN_LENGTH_MIN` is the minimum length a chain of points must be before it can be considered as an edge.

`HALFTHICK` is half the thickness of an edge, in pixels, to erase.

`N_PRE_GUASSIANS` is the number of times to box-blur the original image before looking for any chains.

`ANGLE_INC` is the angle, in radians, that each column represents.

`BLACK` is the color black defined in RGB, in octal.

`WHITE` is the color white defined in RGB, in octal.

`int width, height` is the width and height of the original image in pixels.

`int w_conv, h_conv` is the width and height of the image after it is converted from polar to cartesian coordinates.

`guint8 *orig` is a one-dimensional array containing the intensity values of all the pixels in the original image.

`guint8 *data` is a one-dimensional array corresponding in size to the original image as it is being blurred and manipulated.

`int *chain_data` is a one-dimensional array corresponding in size to the original image of the points marked as chains. When the value is -1, the point belongs to an unknown chain. When the value is 0, the point does not belong to any chain. When the value is positive, the point belongs to the chain of that value.

`guint8 *conv_data` is a one-dimensional array containing the intensity values of all the pixels in the image converted from polar to Cartesian coordinates.

D.4 Function Overview

`static void box_columns()` will box-blur an image in the vertical direction by averaging each pixel with its upper and lower neighbor.

`static void locate_maxima ()` will locate intensity maxima based on the following criteria: it must have an intensity at least half the maximum intensity in the image, its lower and upper neighbors must have a lower intensity. All the points that are found meeting this criteria are stored in `int *chain_data`.

`static int find_closest_nonzero (int *r, int cx, int cy, int w, int h)` searches an array `*r` containing chain data around a pixel located at x=`int cx`, y=`int cy` for values that are non-zero in a search area that is $2w + 1$ wide and $2h + 1$ tall.

`static gboolean find_chains ()` will search through `int *chain_data` for maxima points, connect and label them as chains based on the algorithm of `find_closest_nonzero`. It will also determine the length of each chain. It will return true if there are exactly two chains that are equal to or longer than `CHAIN_LENGTH_MIN`.

`static void link_chain()` joins the nearest horizontal points within a chain with straight lines to form a contiguous chain of pixels.

`static void mask_data ()` determines the upper and lower chain by averaging the vertical position of all the points in the chain. It then turns all the points above the top chain and all the points below the bottom chain of the original image black. It also turns `HALFTHICK` number of points below the top chain and above the bottom chain of the original image black to mask out the thickness of the elastic tube edges.

`static void scan_convert(double theta)` converts the masked, polar coordinate image into Cartesian coordinates. The pixel height of the image remains the same while the width is adjusted based on the total angle that was scanned. To do this, the position of each pixel in the new converted image in the old coordinates is calculated. A linear interpolation of the intensities of the surrounding pixels of the polar coordinate image is used as the intensity for the new pixel.

`int main ()` is, as its name suggests, the main part of the program.

Bibliography

[1] Auerbach, D., Moehring, W., and Moser, M., "An analytical approach to the Liebau problem of valveless pumping," *Cardiovascular Engineering: An International Journal*, vol. 4, no. 2, pp. 201–207, 2004.

[2] Borzi, A. and Propst, G., "Numerical investigation of the Liebau phenomenon," *Zeitschrift für angewandte Mathematik und Physik*, vol. 54, no. 6, pp. 1050–1072, 2003.

[3] Field, S. and Drzewiecki, G. M., "Dynamic response of the collapsible blood vessel," in *Analysis and Assessment of Cardiovascular Function*, pp. 277–296, Springer, 1998.

[4] Fishman, M., "Fashioning the vertebrate heart: Earliest embryonic decisions," 1997.

[5] Forouhar, A., Hickerson, A., Liebling, M., Fraser, S., Dickinson, M., and Gharib, M., "Personal communication: The embryonic zebrafish heart as an impedance pump," 2005.

[6] Grotberg, J. B. and Jensen, O. E., "Biofluid mechanics in flexible tubes," *Annual Review of Fluid Mechanics*, vol. 36, pp. 121–147, 2004.

[7] Hansen, F., Mangell, P., Sonesson, B., and Lanne, T., "Diameter and compliance in the human common carotid-artery — variations with age and sex," *Ultrasound in Medicine and Biology*, vol. 21, no. 1, pp. 1–9, 1995.

[8] Hickerson, A. I., Rinderknecht, D., and Gharib, M., "Experimental study of the behavior of a valveless impedance pump," *Experiments in Fluids*, vol. 38, no. 4, pp. 534–540, 2005.

[9] Hicks, T. G., *Pump Selection and Application*. New York: McGraw-Hill Book Company, Inc., 1957.

[10] Holman, J. P., *Experimental Methods for Engineers*. McGraw-Hill Higher Education, 2001.

[11] Jensen, O., "Instabilities of flow in a collapsed tube," *Journal of Fluid Mechanics*, vol. 220, pp. 623–659, 1990.

[12] Jensen, O. and Pedley, T., "The existance of steady flow in a collapsed tube," *Journal of Fluid Mechanics*, vol. 206, pp. 339–374, 1989.

[13] Jung, E., *Two-Dimensional Simulations of Valveless Pumping Using the Immersed Boundary Method*. PhD thesis, New York University, 1999.

[14] Jung, E. and Peskin, C., "2-D simulations of valveless pumping using immersed boundary methods," *SIAM Journal on Scientific Computing*, vol. 23, no. 1, pp. 19–45, 2001.

[15] Jung, E. and Peskin, C., "2-D simulations of valveless pumping using immersed boundary methods (ii)," 2001.

[16] Kenner, T., Moser, M., Tanev, I., and Ono, K., "The Liebau-effect or on the optimal use of energy for the circulation of blood," *Scripta Medica*, vol. 73, no. 1, pp. 9–14, 2000.

[17] Kenner, T., "Biological asymmetry and cardiovascular blood transport," *Cardiovascular Engineering: An International Journal*, vol. 4, no. 2, pp. 209–217, 2004.

[18] Liebau, G., "Über ein ventilloses Pumpprinzip," *Naturwissenschaften*, vol. 41, p. 327, 1954.

[19] Liebau, G., "Die Stromungsprinzipien des Herzens," *Zeitschrift fr Kreislaufforschung*, pp. 677–684, 1955.

[20] Liebau, G., "Die Bedeutung der Tragheitskrafte dur die Dynamic des Blutkreislaufs," *Zeitschrift für Kreislaufforschung*, pp. 428–438, 1956.

[21] Liley, D., "The physics of doppler ultrasound," 2002.

[22] Mahrenholtz, V. O., "A contribution to the pumping principal of periodically acting valveless pumps," *Forsch. Auf Dem Gebiet des Ingieurwesens*, vol. 29, pp. 47–56, 73–81, 1963.

[23] Moser, M., Huang, J. W., Schwarz, G. S., Kenner, T., and Noordergraaf, A., "Impedance defined flow: Generalization of William Harvey's concept of the circulation - 370 years later," *International Journal of Cardiovascular Medicine and Science*, vol. 1, no. 3/4, pp. 205–211, 1998.

[24] Okamura, S., Suzuki, A., Johkura, K., Ogiwara, N., Yokouchi, T., and Sasaki, K., "Formation of the biopulsatile vascular pump by cardiomyocyte transplants circumvallating the abdominal aorta," *Tissue Engineering*, vol. 8, no. 2, pp. 201–211, 2002.

[25] Olsen, J. H. and Shapiro, A. H., "Large-amplitude unsteady flow in liquid-filled elastic tubes," *Journal of Fluid Mechanics*, vol. 29, no. 3, pp. 513–538, 1967.

[26] Ottesen, J., "Valveless pumping in a fluid-filled closed elastic tube-system: one-dimensional theory with experimental validation," *Journal of Mathematical Biology*, vol. 46, no. 4, pp. 309–332, 2003.

[27] Pontrelli, G., "A mathematical model of flow in a liquid-filled visco-elastic tube," *Medical and Biological Engineering and Computing*, vol. 40, no. 5, pp. 550–556, 2002.

[28] Rao, A. R., "Oscillatory flow in an elastic tube of variable cross-section," *Acta-Mechanica*, vol. 46, pp. 155–165, 1983.

[29] Rath, H. and Teipel, I., "Der Fordereffekt in ventillosen, elastischen Leitungen," *Zeitschrift fr angewandte Mathematik und Physik*, vol. 29, pp. 123–133, 1978.

[30] Rinderknecht, D., Hickerson, A. I., and Gharib, M., "A valveless micro impedance pump driven by electromagnetic actuation," *Journal of Micromechanics and Microengineering*, vol. 15, pp. 861–866, 2005.

[31] Stevanov, M., Baruthio, J., and Eclancher, B., "Fabrication of elastomer arterial models with specified compliance," *Journal of Applied Physiology*, vol. 88, pp. 1291–1294, 2000.

[32] Thomann, H., "A simple pumping mechanism in a valveless tube," *Zeitschrift für angewandte Mathematik und Physik*, vol. 29, pp. 169–177, 1978. Swiss Federal Insititute of Technology, Zurich.

[33] Vogel, S., "Nature's pumps," *American Scientist*, vol. 82, pp. 464–472, 1994.

[34] Wang, D. and Tarbell, J., "Nonlinear analysis of flow in an elastic tube (artery): Steady streaming effects," *Journal of Fluid Mechanics*, vol. 239, pp. 341–358, 1992.

[35] Womersley, J., "Method for the calculation of velocity, rate of flow and viscous drag in arteries when pressure gradient is known," *Journal of Physiology*, vol. 127, pp. 553–563, 1955.

[36] Womersley, J., "Oscillatory motion of a viscous liquid in a thin walled elastic tube: The linear approximation for long waves," *Philosophical Magazine*, vol. 46, no. 373, pp. 199–221, 1955.

[37] Womersley, J., "Oscillatory flow in arteries: The constrained elastic tube as a model of arterial flow and pulse transmission," *Physics in Medicine and Biology*, vol. 2, no. 2, pp. 178–187, 1957.

[38] Womersley, J., "Oscillatory flow in arteries. ii: The reflection of the pulse wave at junctions and rigid inserts in the arterial system," *Physics in Medicine and Biology*, vol. 2, no. 4, pp. 313–323, 1958.

[39] Womersley, J., "Oscillatory flow in arteries. iii: Flow and pulse-velocity formulae for a liquid whose viscosity varies with frequency," *Physics in Medicine and Biology*, vol. 2, no. 4, pp. 374–382, 1958.

[40] Zhang, Y., Reese, J., Gorman, D., and Madhok, R., "The vibration of an artery-like tube conveying pulsatile fluid flow," *Proceeding of the Institution of Mechanical Engineers Part H — Journal of Engineering in Medicine*, vol. 216, no. H1, pp. 1–11, 2002.